Endothelin B receptor inhibition rescues aging-dependent neuronal regenerative decline

Rui Feng[1], Sarah F. Rosen[1], Irshad Ansari[1], Sebastian John[1], Michael B. Thomsen[2], Cedric G. Geoffroy[3] and Valeria Cavalli[1,4,5*]

[1] Department of Neuroscience, Washington University School of Medicine, St. Louis, MO 63110, USA.

[2] CS27 LLC, Springboro, OH, USA.

[3] Department of Neuroscience & Experimental Therapeutics, Texas A&M Health Science Center, Bryan, TX, 77807, USA

[4] Center of Regenerative Medicine, Washington University School of Medicine, St. Louis, MO 63110, USA.

[5]Hope Center for Neurological Disorders, Washington University School of Medicine, St. Louis, MO 63110, USA.

*Correspondence to: cavalli@wustl.edu

Valeria Cavalli, Department of Neuroscience, Washington University School of Medicine,

MSC: 8108-12-922, 660 South Euclid Avenue, St. Louis, MO 63110-1093.

Phone: +1(314)362-3540, Fax: +1(314)362-3446.

One Sentence Summary:

Inhibition of endothelin signaling improves nerve regeneration after central and peripheral injuries and counters age-related regenerative decline.

Abstract:

Peripheral sensory neurons regenerate their axons after injury to regain function, but this ability declines with age. The mechanisms behind this decline are not fully understood. While excessive production of endothelin 1 (ET-1), a potent vasoconstrictor, is linked to many diseases that increase with age, the role of ET-1 and its receptors in axon regeneration is unknown. Using a single cell RNAseq approach, we reveal that in dorsal root ganglia (DRG), satellite glial cells (SGCs), which completely envelop the sensory neuron soma, express the endothelin B receptor (ETBR), while ET-1 is expressed by endothelial cells. Inhibition of ETBR *ex-vivo* in DRG explant cultures improves axon growth in both adult and aged conditions. *In vivo,* treatment with the FDA-approved compound, Bosentan, improves axon regeneration and reverses the age-dependent decrease in axonal regenerative capacity. Bosentan treatment also enhances the expression of connexin 43 in SGCs after injury in adult and aged mice. These results reveal that inhibiting ETBR function enhances axon regeneration and rescues the age-dependent decrease in axonal regenerative capacity, providing a potential avenue for future therapies.

Keywords:

Dorsal root ganglion (DRG), Endothelin B receptor (ETBR), Bosentan, Satellite glial cells (SGCs), Axon regeneration, Nerve injury, Aging.

18 **INTRODUCTION**

19 Peripheral nerve injuries, resulting from traumatic injuries, lesions, degenerative diseases,
20 and neuropathies, have a major impact on patient's functioning and quality of life (Maita et al.,
21 2023). While neurons in the peripheral nervous system regenerate their axons after nerve injury,
22 functional recovery remains very limited because of the slow growth rate of axons and the often
23 long distances that growing axons face to reconnect with their initial targets (Hoke, 2006).
24 Unfortunately, the ability of injured neurons to regenerate their axons declines with age (Pestronk
25 et al., 1980; Vaughan, 1992; Verdu et al., 2000), contributing to increases in healthcare costs and
26 the risk of long-term disability (Pestronk et al., 1980; Vaughan, 1992; Verdu et al., 2000; Yun,
27 2015). Thus, discovery of therapeutics that promote axon regeneration and counter age-related
28 decline in regenerative capacity is vital.

29 Primary sensory neurons, with their cell soma located in the dorsal root ganglia (DRG),
30 convey sensory information from peripheral tissue to the brain via the spinal cord, and represent
31 a useful model to identify the molecular and cellular mechanisms that promote axon regeneration.
32 After injury, successful axonal regeneration of sensory neurons requires activation of neuronal-
33 intrinsic epigenetic, transcriptional, and translational programs (He and Jin, 2016; Mahar and
34 Cavalli, 2018; Rishal and Fainzilber, 2014; Tedeschi and Bradke, 2017). Additionally, non-
35 neuronal cells at the site of injury and in the DRG play an important role in axon regeneration after
36 injury. Satellite glial cells (SGCs) surrounding the cell soma (Avraham et al., 2020; Avraham et
37 al., 2021; Jager et al., 2020) and Schwann cells surrounding the axon (Jessen and Mirsky, 2016),
38 undergo changes in transcriptional states that support axon regeneration. Macrophages recruited
39 to the nerve (Ydens et al., 2020; Zigmond and Echevarria, 2019), and macrophages proliferating
40 in the DRG (Feng et al., 2023) also contribute to axon regeneration after injury.

41 During aging, decreases in the efficiency of the axonal transport system (Andrews et al.,
42 2016; Black and Lasek, 1979), mitochondrial function (Sutherland et al., 2021), and epigenetic

43 and transcriptional mechanisms (Li et al., 2010) limit the regenerative capacity of neurons.
44 Increases in pro-inflammatory cytokines and macrophage infiltration into the peripheral nerve
45 (Buttner et al., 2018), as well as an increased numbers of T cells in the DRG, have been shown
46 to contribute to the limited regenerative capacity of neurons in aged mice (Zhou et al., 2022).
47 Additionally, age-related decline in the de-differentiation, activation, and senescence of Schwann
48 cells hampers axonal re-growth in damaged peripheral nerves (Fuentes-Flores et al., 2023; Kang
49 and Lichtman, 2013; Painter et al., 2014). While changes in SGCs morphology (Pannese et al.,
50 1996), as well as changes in SGCs-neuronal coupling have been reported with age (Huang et al.,
51 2006; Procacci et al., 2008), the contribution of SGCs to age-dependent decreases in axonal
52 regenerative capacity have not been investigated.

53 Connexin 43 (Cx43) is the most highly expressed member of the connexin family in SGCs
54 (Avraham et al., 2022; Huang et al., 2005) and its expression decreases during aging (Procacci
55 et al., 2008). Studies in astrocytes, which share many functional and molecular features with
56 SGCs (Avraham et al., 2022; Avraham et al., 2020; Hanani and Verkhratsky, 2021) have shown
57 that endothelin 1 (ET-1) signaling via the endothelin receptor B (ETBR) inhibits the expression of
58 Cx43 and reduces gap junction mediated coupling (Blomstrand et al., 2004; Rozyczka et al.,
59 2005). In cultured SGCs, ET-1 also reduces gap junction coupling (Feldman-Goriachnik and
60 Hanani, 2017). ET-1 is a potent vasoconstrictor secreted by endothelial cells and is the
61 predominant isoform of endothelin in the human cardiovascular system (Luscher and Barton,
62 2000; Yanagisawa et al., 1988). ET-1 production increases with age and is linked to many age-
63 associated diseases (Barton, 2014; Jankowich and Choudhary, 2020; Stauffer et al., 2008). ET-
64 1 signaling was also suggested to play a role in pain (Khodorova et al., 2009; Pomonis et al.,
65 2001). Whether endothelin signaling contributes to axon regeneration and age-dependent axon
66 regenerative decline has not been examined.

67 To determine the role of endothelin signaling in axon regeneration during aging, we
68 performed unbiased single-cell RNA-sequencing of the DRG cells from mice 3 months of age
69 (adult), 12 months of age (middle-aged) and 21 months of age (aged). Examination of endothelins
70 and their receptors revealed enrichment of *Edn1* in endothelial cells and *Ednrb* in SGCs. Inhibition
71 of ETBR using the selective antagonist BQ788 in DRG explant cultures enhanced axonal
72 outgrowth in adults and restored axonal regenerative capacity in aged conditions. Treatment of
73 adult and aged mice with Bosentan, an FDA-approved ETBR/ETAR antagonist (Clozel et al.,
74 1994), improved axon regeneration after peripheral nerve injury. Bosentan treatment also
75 increased expression of Cx43 in SGCs after injury in adult and age mice. These results suggest
76 that ETBR signaling inhibits axon regeneration after nerve injury and plays a role in age-related
77 decline in regenerative capacity. Thus, ETBR antagonism may be a potential therapeutic avenue
78 to enhance axon growth after nerve injury and to restore axon regenerative capacity that declines
79 with age.

80 **RESULTS**

81 ***Ednrb* is highly expressed in SGCs.**

82 The dense vascularization of the DRG cell body area coupled with the high permeability
83 of these capillaries in rodents and human (Godel et al., 2016; Jimenez-Andrade et al., 2008)
84 suggests that neurons and their surrounding SGCs may be influenced by vascular-derived signals.
85 Whole mount preparation of DRG from Lycopersicon Esculentum Lectin (LEL) injected
86 *Fabp7*^{CreER}::Ai14 mouse, which labels SGCs with tdTomato (Avraham et al., 2020) revealed the
87 dense vascularization in the neuronal soma rich area of the DRG, as previously reported
88 (Jimenez-Andrade et al., 2008) (Fig.1A). Additionally, immunofluorescent staining of neurons and
89 SGCs in the DRG from LEL injected adult mouse demonstrated that blood vessels are closely
90 juxtaposed to SGCs surrounding sensory neuron somas (Fig.1B).

91 To understand the role of endothelin intercellular signaling pathways in the DRG
92 microenvironment during aging, we performed single cell RNA sequencing (scRNA-seq) on
93 lumbar DRGs from mice 3 months of age (adult), 12 months of age (middle-aged) and 21 months
94 of age (aged) using the Chromium Single Cell Gene Expression Solution (10 X Genomics), as
95 described previously (Avraham et al., 2022; Avraham et al., 2020; Avraham et al., 2021). We
96 sequenced a total of 18,098 cells (16,923 adult, 602 mid-aged, 573 old) from two biological
97 replicates per age with an average of 3,411 genes and 12,071 transcripts detected per cell (see
98 methods for filtering criteria). Following condition integration and unsupervised clustering, we
99 identified 8 major clusters containing cells from all age groups (Fig 1C). Examination of cluster-
100 specific marker genes revealed major cellular subtypes including endothelial cells (*Flt1, Pecam1*),
101 SGCs (*Fabp7, Ptprz1*), fibroblasts (*Col1a1, Dcn*), non-myelinating Schwann Cells (*Scn7a*, *Ntrk3*),
102 myelinating Schwann cells (*Mpz, Ncmap*), neurons (*Prph, Tac1*), mural cells (*Rgs5, Notch3*), and
103 macrophages (C1qa, *Aif1*) (Fig.1D, Supplementary Fig.1A, Supplementary File 1 related to Fig.1).
104 *Ednrb* was highly enriched in SGCs, with lower levels of expression in non-myelinating and
105 myelinating Schwann cells (Fig.1F), whereas *Ednra* was expressed mainly in Mural cells (Fig.1E).
106 *Ednrb* enrichment in SGCs is consistent with prior studies (Mapps et al., 2022; Pomonis et al.,
107 2001; Tasdemir-Yilmaz et al., 2021). Endothelin-1 (*Edn1*) and endothelin-3 (*Edn3)* were
108 expressed in endothelial cells and fibroblasts, respectively, whereas *Edn2* was not detected (Fig
109 1G, Supplementary Fig.1A). *Ednrb* levels decreased with age, whereas *Edn1* increased with age
110 (Supplementary Fig.1B). *Ednrb* mRNA in SGCs was validated by RNA *in situ* hybridization, which
111 showed *Ednrb* co-localized with the SGCs marker *Fabp7* (Avraham et al., 2020) (Fig.1H). Using
112 our previously generated scRNAseq data sets (Avraham et al., 2022), we also found that *Ednrb*
113 is highly expressed in SGCs in rat, and exclusively expressed in SGCs in humans (Supplementary
114 Fig.1C,D).

115 **Endothelin B receptor inhibition increases axonal growth *in vitro* and *ex vivo.***

116 To investigate the role of ETBR signaling in axonal growth, we used different compounds
117 to inihibit or activate endothelin receptors in dissociated L4-L5 DRG mixed cultures. Adult DRG
118 mixed cultures, containing neuronal and non neuronal cells, were plated and treated with an
119 ETBR antagonist (BQ788), ETBR agonist (IRL1620), endothelin A receptor (ETAR) antagonist
120 (BQ123), or vehicle for 24 hours. Neurons were then labeled with antibodies against beta III
121 tubulin (TUJ1) and axonal radial length was quantified. Antagonism of ETBR with BQ788
122 significantly increased axonal radial length compared to vehicle (Fig.2A-C). However, agonism of
123 ETBR with IRL1620 or antagonism of ETAR with BQ123 had no significant effects on axonal
124 radial length compared to vehicle treatment (Fig.2A-C). These results indicated that ETBR
125 signaling inhibits axonal growth *in vitro*.

126 To further examine the role of ETBR antagonism on axonal growth, we used DRG explants
127 in which L3-L5 DRGs from adult mice were seeded in matrigel and cultured for 7 days (Feng et
128 al., 2023). Explants were then treated with vehicle or BQ788 at days in vitro (DIV) 1 and radial
129 axon growth was assessed at DIV7 by measuring the length of 50 or more axons per explant.
130 Radial axon growth was significantly increased in explants treated with BQ788 compared to
131 vehicle treatment (Fig.2D-F). To confirm that the *in vivo* morphology of SGCs enveloping neuronal
132 somas was intact, DRG explants were immunostained with TUJ1 for neurons and FABP7 for
133 SGCs at DIV 7 (Fig 2G). These results further confirmed that ETBR signaling inhibits axon growth
134 in an *ex-vivo* model.

135 **Bosentan treatment improves axon regeneration after nerve injury.**

136 To determine the potential role of ETBR in regulating nerve regeneration *in vivo*, we used
137 our established *in-vivo* and *ex-vivo* regeneration assays (Avraham et al., 2020; Cho and Cavalli,
138 2012; Cho et al., 2015; Cho et al., 2013) in combination with the FDA-approved compounds that
139 antagonize endothelin receptors, Bosentan and Ambrisentan. These compounds have been
140 utilized to treat pulmonary arterial hypertension, and their safety and efficacy have been

141 demonstrated through various clinical trials (Chen et al., 2018; Galie et al., 2008; Peacock et al.,
142 2015; Rubin et al., 2002). Bosentan is an antagonist of both ETAR and ETBR (Clozel et al., 1994),
143 while Ambrisentan is an antagonist selective for ETAR (Humbert et al., 2004; Newman et al.,
144 2007). Adult mice were treated orally with vehicle, Bosentan or Ambrisentan 2 hours prior to
145 receiving a sciatic nerve crush (SNC) injury. Axon regeneration was assessed 24 hours after
146 injury by measuring the intensity of SCG10 labeled axons, a marker for regenerating axons (Shin
147 et al., 2014) (Fig.3A-E). SCG10 intensity was measured distal to the crush site, which was
148 determined according to the highest SCG10 intensity along the nerve (Avraham et al., 2020; Cho
149 et al., 2013; Feng et al., 2023; Shin et al., 2014) and axon elongation was quantified by
150 measurement of the 10 longest axons, as previously described (Carlin et al., 2019) (Fig.3B). A
151 50% regeneration index was quantified by normalizing the average SCG10 intensity at distances
152 away from the crush site to the SCG10 intensity at the crush site, to account for both the length
153 and number of regenerating axons past the crush site and plotting the distance at which SCG10
154 intensity is half of that at the crush site (Cho et al., 2013; Feng et al., 2023) (Fig.3C). Mice that
155 received Bosentan had significantly longer axons and a higher 50% regeneration index 1 day
156 after SNC compared to mice that received vehicle, whereas mice that received Ambrisentan had
157 no significant differences in axon regeneration compared to vehicle (Fig.3B-D). Quantification of
158 the percentage of SCG10 intensity normalized to the crush site at several distances from the
159 injury was also greater in Bosentan treated mice compared to vehicle (Fig.3E). Similarly, at 3 days
160 post SNC, mice that received Bosentan 2 hours before SNC, and then every 24 hours, had
161 improved axon regeneration compared to vehicle, whereas mice that received Ambrisentan had
162 no significant differences in axon regeneration compared to vehicle (Supplementary Fig.2A-E).
163 Examination of *Edn1, Ednra, and Ednrb* mRNA by RT-qPCR and ETBR by western blot in non-
164 treated mice showed no significant differences in mRNA or protein levels at 3 days post SNC
165 compared to control (Supplementary Fig.2F-H). These results suggest that, although ETBR levels

166 do not change after injury, ETBR antagonism increases axon regeneration after peripheral nerve
167 injury at both 1 and 3 days.

168 We next tested if inhibition of ETBR influences the conditioning injury paradigm, in which
169 a prior nerve injury increases the growth capacity of neurons (Smith and Skene, 1997). DRG
170 neurons from mice that received Bosentan or Ambrisentan 2 hours before SNC, and then every
171 24 hours for three days, were cultured and axon growth capacity was quantified by measuring the
172 axon radial length and TUJ1 positive area (Fig.3G-I). In uninjured condition, neurons extend short
173 neurites, whereas a prior nerve injury leads to neurons growing longer neurites (Fig 3G,H), as
174 expected (Smith and Skene, 1997). Bosentan, but not Ambrisentan, enhanced the axon radial
175 length of DRG neurons cultured from uninjured adult mice, partially mimicking the conditioning
176 injury, and also increased the growth capacity of injured neurons (Fig.3G,H). Since the selective
177 ETAR antagonists, BQ123 and Ambrisentan, had no significant effects on axon growth
178 regeneration after nerve injury (Fig 2A-C, 3A-E), our results indicate that ETBR limits axon
179 regeneration capacity.

180 To determine the effects of Bosentan treatment on axon regeneration in a model with
181 lower regenerative capacity, axon growth after dorsal root crush (DRC) injury was assessed
182 (Supplementary Fig.3A). Following DRC injury, axon growth occurs at about half the rate of
183 peripheral axons (Oblinger and Lasek, 1984; Wujek and Lasek, 1983) and our previous work has
184 shown that manipulation of SGCs after DRC improves axon regeneration (Avraham et al., 2021).
185 Axon regeneration at 3 days post DRC was assessed by measuring SCG10 intensity, as
186 described above. Mice that received Bosentan had significantly more axon regeneration along
187 the dorsal root compared to vehicle (Supplementary Fig.3B-E). Together, these results indicate
188 that ETBR inhibition improves axon regeneration after both peripheral and central axon injury in
189 DRG neurons.

190

191 **Inhibiting ETBR rescues aging-dependent axonal regenerative decline.**

192 To determine the role of ETBR signaling on axon growth during aging, DRG explants from
193 aged (21-month-old) mice were treated with BQ788 or vehicle (Fig.4A). Aged DRG explants
194 treated with BQ788 had significantly increased radial axon length compared to vehicle (Fig.4B-
195 C). In fact, aged explants treated with BQ788 had significantly more radial axon growth than to
196 that of adult (3-month old) vehicle explants (Fig 4C). Axon regeneration after peripheral nerve
197 injury in aged mice was also assessed by measuring SCG10 intensity in adult and aged mice 3
198 days post SNC. As expected, aged vehicle-treated mice had significantly less axon regeneration
199 compared to adult vehicle-treated mice (Fig 4D-G) (Zhou et al., 2022). However, aged mice
200 treated with Bosentan had significantly increased axon regeneration compared to vehicle-treated
201 aged mice. Indeed, treatment with Bosentan increased axon regeneration in aged mice to levels
202 similar to vehicle-treated adult mice (Fig.4D-G). These results indicate that inhibition of ETBR
203 rescues the age-dependent decline in axon regeneration.

204 **ETBR inhibition increases the expression of Cx43 in SGCs in adult and aged mice.**

205 Cx43 is a member of the connexin family and can form hemichannels and gap junction
206 channels (Mazaud et al., 2021). Several studies suggest that both Cx43 gap junctions and
207 hemichannels operate in SGCs and have an important role in communication between SGCs and
208 sensory neurons (Hanani and Spray, 2020; Retamal et al., 2017). Past studies in mice have also
209 shown that Cx43 expression in SGCs decreases during aging (Procacci et al., 2008), while both
210 the number of gap junctions and the dye coupling between these cells increases (Huang et al.,
211 2006). Our scRNA-sequencing data revealed that *Gja1*, the gene for Cx43, is enriched in SGCs
212 in both mice and human (Fig.5A,B) (Avraham et al., 2022) and that *Gja1* in SGCs decreased with
213 age in mice (Fig.5C). In contrast, *Gjc1,* the gene for Cx45 displayed a trend of increased
214 expression with age (Fig.5C), suggesting that Cx45 may contribute to the previously observed
215 increase in gap junction (Huang et al., 2006). At the protein level, Cx43 is highly expressed in

216 SGCs in mice (Fig.5G and Movie S1). The level of Cx43 expression, measured by both the Cx43
217 expression area and the number of Cx43 puncta in Fabp7 positive SGCs surrounding neuron,
218 was significantly lower in aged mice compared to adult mice (Fig.5E-G), consistent with prior
219 studies (Ohara et al., 2008; Procacci et al., 2008).

220 In cultured SGCs and astrocytes, endothelin signaling reduces the expression Cx43
221 (Blomstrand et al., 2004; Feldman-Goriachnik and Hanani, 2017; Rozyczka et al., 2005), while
222 nerve injury increases SGCs gap junction coupling (Hanani et al., 2002; Kim et al., 2016; Pannese
223 et al., 2003). To elucidate a potential mechanism by which ETBR antagonism increases axonal
224 regeneration, the effect of Bosentan treatment on expression of Cx43 in SGCs was assessed.
225 Cx43 expression level on SGCs was increased 3 days after SNC in both adult and aged vehicle-
226 treated mice (Fig.5E-G). Bosentan treatment led to an increase in Cx43 expression in both adult
227 and aged mice (Fig.5E-G). Examination of Cx43 expression in SGCs after DRC in adult mice
228 showed no increase in Cx43 levels compared to uninjured mice, but Bosentan-treated mice
229 increased Cx43 levels compared to vehicle (Supplementary Fig.4A-C). These results
230 demonstrate that Bosentan treatment increases Cx43 expression in SGCs, providing a possible
231 mechanism by which ETBR inhibition promotes axon regeneration after injury.

232

233 **Aging alters SGCs morphology and metabolism.**

234 Changes in morphology of SGCs have been reported with age, with a decrease in SGCs
235 number and SGCs retracting and leaving the neuronal soma exposed to the extra cellular DRG
236 environment in aged rabbit (Pannese et al., 1997; Pannese et al., 1996). In the DRG of aged mice,
237 neurons are usually enveloped by their own sheath of SGCs (Huang et al., 2006). We thus
238 examined the impact of age on SGCs morphology by transmission electron microscopy (TEM).
239 In adult mice, each sensory neuron was enveloped by its own SGCs sheath as described
240 previously (Pannese, 1981, 2010). In aged mice, SGCs appeared thinner compared to adult mice

241 (Fig 6A). Quantification of the average width of SGCs per neuron demonstrated a significant
242 decrease during aging (Fig.6B). Quantification of the total number of SGCs nuclei per neuron
243 soma in TEM images revealed that 21-month-old mice had a higher frequency of neurons with 0
244 or 1 SGC nuclei per neuron than 2-month-old mice (Fig.6C), suggesting a decrease in SGCs
245 number around neuron soma with age. These results suggest that SGCs may undergo atrophy
246 or senescence during aging, consistent with the hypothesis that a prominent decrease in Cx43 is
247 a marker of senescence (Procacci et al., 2008).

248 To further examine the gene expression changes during aging, we performed differential
249 gene expression analysis to identify common patterns of aging gene expression in mid-aged and
250 aged samples across all cell types. Due to fewer cells recovered from mid-aged and old DRG
251 samples, all cell types were pooled for DEG analysis. A considerable number of genes were
252 differentially expressed when comparing mid-aged to adult (1977 upregulated, 3968
253 downregulated), and old to adult (1768 upregulated, 4053 downregulated) samples, with
254 substantial overlap between the two aged groups (Fig.6D-F, Supplementary File 2 related to
255 Fig.6). Kyoto Encyclopedia of Genes and Genomes (KEGG) pathway and Gene Ontology (GO)
256 analysis for the DEGs overlapping in mid-aged or aged groups compared to adults revealed
257 upregulation of a limited number of pathways including Rap1 signaling and ribosome function (Fig
258 6G, Supplementary Fig.5B-C). Conversely, the pathways and terms identified from the set of
259 downregulated genes were numerous (Fig.6H, Supplementary File 3 related to Fig.6).
260 Interestingly, the strongest downregulated pathways in aged samples were related to fatty acid
261 and cholesterol metabolism, as well as PPARα (Fig.6H). Our previous studies have shown that
262 fatty acid metabolism upstream of PPARα in SGCs promotes axon regeneration (Avraham et al.,
263 2020; Avraham et al., 2021), suggesting that in addition to a reduction in Cx43, a decrease in fatty
264 acid metabolism and PPARα signaling in SGCs may contribute to age-dependent regenerative
265 decline.

266

267 **DISCUSSION**

268 Peripheral nerve injuries have a major impact on patient's functioning and quality of life
269 (Maita et al., 2023). The ability of injured neurons to regenerate their axons declines with age
270 (Geoffroy et al., 2016; Geoffroy et al., 2017; Pestronk et al., 1980; Vaughan, 1992; Verdu et al.,
271 2000), contributing to increase the risk of long-term disability (Pestronk et al., 1980; Vaughan,
272 1992; Verdu et al., 2000; Yun, 2015). Our study showed that ETBR functions in part to limit axon
273 regenerative capacity and that Bosentan, an FDA-approved ETBR/ETAR antagonist, increased
274 axonal regeneration after peripheral and central axon nerve injury. Furthermore, Bosentan
275 rescued the age-dependent decrease in axonal regenerative capacity. These results suggest that
276 ETBR inhibition may be a beneficial therapeutic to promote axon regeneration after injury.

277 Our results demonstrate that *Ednrb* is highly enriched in SGCs in the DRG, and selective
278 antagonism of ETBR in DRG explants increases axon outgrowth, suggesting that Bosentan
279 treatment increases axon growth after nerve injury via inhibition of ETBR on SGCs. It is important
280 to note that, in the nerve, ETBR is also expressed on Schwann cells and has been shown to play
281 a role in Schwann cell generation (Brennan et al., 2000). Thus, we cannot rule out that Bosentan
282 treatment *in vivo* may also promote axon regeneration through ETBR on Schwann cells. However,
283 as DRG explants maintain the SGC-sensory neuron morphology and axon outgrowth in this model
284 does not rely on repair Schwann cells, we can conclude that blocking ETBR signaling in SGCs
285 significantly contributes to axon outgrowth. As our sequencing data showed that *Edn1/*ET-1, a
286 ligand for ETBR, is enriched in endothelial cells, and there is a dense and permeable
287 vascularization in the DRG, we hypothesize that ET-1 arises from endothelial cells lining blood
288 vessels. However, other studies have suggested that ET-1 is also expressed by small diameter
289 neurons (Giaid et al., 1989), thus it is possible that ET-1 from neurons is also acting on ETBR in
290 SGCs. The observation that elevated tissue or plasma concentrations of ET-1 occurs with age

291 (Jankowich and Choudhary, 2020) supports our results that ETBR functions to limit axon
292 regenerative capacity in aged mice.

293 Cx43 is a transmembrane protein that performs canonical gap junction functions, such as
294 connecting adjacent cells and allowing the diffusion of ions and small molecules. Cx43 can also
295 form hemichannels that have an important role in communication between SGCs and sensory
296 neurons (Retamal et al., 2017). Published work from our lab and others, as well as the current
297 study, show that Cx43 is the most abundant member of the connexin family in SGCs and its
298 expression increases following nerve injury (Avraham et al., 2021; Hanani and Spray, 2020) and
299 decreases with age (Procacci et al., 2008). In the current study, Cx43 in SGCs from both adult
300 and aged injured mice were increased with Bosentan treatment compared to vehicle treatment.
301 Studies in cultured SGCs and astrocytes have demonstrated that endothelin signaling reduces
302 gap junctions coupling (Blomstrand et al., 2004; Feldman-Goriachnik and Hanani, 2017;
303 Rozyczka et al., 2005)(Blomstrand et al., 2004). Mechanistically, we thus hypothesize that ETBR
304 inhibition in SGCs contributes to axonal regeneration by increasing Cx43 levels, gap junction
305 coupling or hemichannels and facilitating SGC-neuron communication. In astrocytes, connexins
306 hemichannels also regulate astrocyte volume (Quist et al., 2000) and adhesive contacts (Cotrina
307 et al., 2008). The decrease in Cx43 expression in aged mice may thus contribute to the decrease
308 SGCs volume we observed, and is consistent with the hypothesis that a prominent decrease in
309 Cx43 is a marker of senescence (Procacci et al., 2008). Emerging evidence also suggest that
310 connexins can perform non-channel functions, such as protein interaction, cell adhesion, and
311 intracellular signaling (Mazaud et al., 2021). Future studies are aimed at determining the
312 mechanisms by which the ETBR and Cx43 in SGCs regulate axon regeneration.

313 In our previous studies, we showed that PPARα signaling downstream of fatty acid
314 synthase in SGCs promotes axon regeneration, in part via regulation of pro-regenerative genes
315 expression in neurons (Avraham et al., 2020; Avraham et al., 2021). In the current study, pathway

316 analysis of transcriptional changes in the DRG during aging revealed downregulation of pathways
317 related to lipid metabolism and fatty acid synthesis. This result suggests that reduction in lipid
318 metabolism in SGCs may contribute to age related decline in axon regeneration in addition to the
319 ETBR-Cx43 axis. Our data also indicate that the number of SGCs surrounding each soma
320 decreases with age, suggesting SGCs loss in addition to SGCs atrophy with age may be linked
321 to the neuronal loss observed with age (Nagashima and Oota, 1974). In addition to loss of support,
322 aged SGCs may also transition into a senescent phenotype that limit axon regeneration.
323 Senescence of Schwann cells in aged mice was shown to undermine axonal regeneration, and
324 systemic elimination of senescent cells with senolytic drugs improves axonal regeneration
325 (Fuentes-Flores et al., 2023), raising the interesting possibility that senescent SGCs also
326 contribute to limit axon regeneration in aged mice. Future studies are needed to determine if aged
327 SGCs, similarly to aged Schwann cells, secrete inhibitory factors that limit axon regeneration.

328 Taken together, our results suggest that ETBR signaling inhibits axon regeneration after
329 nerve injury and contributes to age-related decreases in neuronal regenerative capacity.
330 Bosentan, an FDA approved ETBR/ETAR antagonist, significantly increased axon regeneration
331 in both adult and aged mice, suggesting a potential therapeutic avenue that may be used to
332 enhance axonal regeneration after nerve injury.

333 **MATERIALS AND METHODS**

334 **Study design**

335 The main goals of this study were to investigate the role of ETBR in axonal regeneration,
336 explore its impact on SGCs in the DRG, and evaluate the therapeutic potential of Bosentan, an
337 FDA-approved drug, on axon regeneration and age-related decline capacity for nerve repair. We
338 performed scRNA-seq analysis on DRG samples from adult, mid-age, and aged mice, along with
339 comparisons to previous datasets. To achieve these objectives, we conducted single-cell RNA

340 sequencing (scRNA-seq) analysis on samples collected from 2-3-month-old (adult), 12-month-old
341 (mid-age), and 21-month-old (aged) mice. Two biological duplicates were utilized and compared
342 with our previous dataset (Avraham et al., 2021). Rat single-cell and Human single-nucleus RNA
343 sequencing (snRNA-seq) data were obtained from our previous dataset (Avraham et al., 2022)
344 Considering that the previous mouse datasets only involved female mice, we exclusively
345 employed female mice for scRNA-seq in the mouse samples. We analyzed samples from mice
346 subjected to various treatments and performed *in vitro* assays including immunofluorescence (IF),
347 Western blotting, quantitative real-time polymerase chain reaction (qPCR), and RNA *in situ*
348 hybridization (RNAscope). For *in vitro* cell assays, data were collected from at least three
349 independent cultures, as indicated in figure legends. *In vivo* experiments were conducted using
350 biological replicates, as denoted by the 'n' values in the figure legends. The sample sizes were
351 determined based on previous experience for each experiment, and mice were randomly
352 assigned to the experimental groups whenever possible. No mice, outliers, or other data points
353 were excluded. Details on animal assignment, randomization, and blinding in different
354 experiments are found in the corresponding sections describing each experiment in Materials and
355 Methods.

356 **Animals**

357 Mice of different age groups were included in the study, specifically 2-3-month-old (adult,
358 female and male), 12-month-old (mid-age, female), and 21-month-old (aged, female). Wild-type
359 C57BL/6 mice were purchased from Envigo (Envigo #027) and Jackson Laboratory (Stock No:
360 000664). Ai14 (B6.Cg-Gt(ROSA)26Sortm14(CAG-tdTomato)Hze/J, JAX Stock No: 007914) mice
361 was obtained from The Jackson Laboratory (Madisen et al., 2010). The *Blbp*^{CreER} (*Fabp7*^{CreER})
362 mouse line was a generous gift from Dr. Toshihiko Hosoya (Maruoka et al., 2011). Ai14 mice were
363 crossed with *Fabp7*^{CreER} mice to obtain *Fabp7*^{CreER}::Ai14 mice. Mice were housed in the animal
364 facility at Washington University in St. Louis, where temperature (64-79°F) and humidity (30%-

365 70%) were carefully controlled. They were socially housed in individually ventilated cages, with
366 1-5 mice per cage, and subjected to a 12-hour light/dark cycle (6 am/6 pm). Mice had unrestricted
367 access to food and water throughout the study. All experimental procedures were conducted
368 following the approved protocol (21-0104) by the Institutional Animal Care and Use Committees
369 of Washington University in St. Louis. All experiments adhered to relevant guidelines and
370 regulations. The study obtained approval from the Washington University School of Medicine
371 Institutional Animal Care and Use Committee (IACUC) under protocol A-3381-01. The mice were
372 housed and cared for in the animal care facility at Washington University School of Medicine,
373 which is accredited by the Association for Assessment & Accreditation of Laboratory Animal Care
374 (AALAC) and complies with the PHS guidelines for Animal Care. The facility has been accredited
375 since 7/18/97, and its USDA Accreditation Registration number is 43-R-008.

376 **Primary adult DRG culture**

377 L4 and L5 DRGs were collected from 12-week-old mice and placed in cold dissection
378 medium composed of HBSS (Thermo Fisher, Gibco; Catalog#: 14175-079) with 10% 1M HEPES
379 (Thermo Fisher, Gibco; Catalog#: 15630080). The DRGs were then transferred to freshly
380 prepared pre-warmed dissociation medium containing 15U/mL Papain suspension (Worthington
381 Biochemical; Catalog#: LS003126), 0.3mg/mL L-cysteine (Sigma; Catalog#: C7352), 0.1mg/mL
382 Deoxyribonuclease I (Worthington Biochemical; Catalog#: LS002139), and 10% 1M HEPES in
383 HBSS. The samples were incubated at 37°C for 20 minutes. After washing the samples twice with
384 pre-warmed HBSS, collagenase (150μg/mL; Sigma; Catalog#: C6885) was added, and the
385 samples were incubated at 37°C for another 20 minutes. Following two additional washes with
386 pre-warmed HBSS, the resulting single-cell suspension was gently triturated and resuspended in
387 complete medium consisting of Neurobasal™-A Medium (Thermo Fisher, Gibco; Catalog#:
388 12349015) supplemented with B-27™ Plus Supplement (Thermo Fisher, Gibco; Catalog#:
389 A3582801) and GlutaMAX™ Supplement (Thermo Fisher, Gibco; Catalog#: 35050061). The cell

390 suspension was then passed through 70-micron cell strainers. The single-cell suspension was
391 then centrifuged at 500 × rpm at 4°C for 5 minutes, and the cell pellet was resuspended in
392 complete Neurobasal medium. Cells were seeded on poly-D-lysine (PDL)-coated 18mm
393 coverslips at a density of 1.0 × 10^3 cells per coverslip. For drug treatment, BQ788 (Sigma;
394 Catalog #B157) 1μM, BQ123 (R&D system; Catalog #: 1188) 1mM, IRL620 (Sigma; Catalog #:
395 SCP0135) 100nM or DMSO as vehicle control were added directly to the complete medium just
396 before suspending the cells and seeding them into separate culture plates and incubated for the
397 entire 24-hour culture period. The animals were randomized into groups and the researcher was
398 not blinded during the analysis.

399 **DRG Explant culture**

400 L3-L5 DRGs from male and female 8-wk- or 21-wk- old mice were collected into cold
401 dissection medium [HBSS (Thermofisher, Gibco; Catalog#:14175-079)] with 10% 1M HEPES
402 (Thermofisher, Gibco; Catalog#15630080) and 18 mM D-Glucose (Sigma; Catalog# G7021).
403 DRG roots were trimmed to 2mm with a sharp scalpel, then seeded on PDL/ laminin-coated cell
404 culture plates. 24 hours after plating, the media was removed and replaced with vehicle (0.1%
405 DMSO) or BQ788 (1μM) in complete medium (Neurobasal™-A Medium, Thermofisher, Gibco;
406 Catalog# 12349015) with B-27™ Plus Supplement (Thermofisher, Gibco; Catalog# A3582801);
407 GlutaMAX™ Supplement (Thermofisher, Gibco; Catalog#35050061), and 2.5% Fetal Bovine
408 Serum (FBS) (Gibco, Catalog#A31604). 7 days after plating, explants were fixed and stained for
409 immunofluorescence.

410 **Sciatic nerve and dorsal root injuries**

411 Sciatic nerve crush injuries were performed following established protocols (Avraham et
412 al., 2021). Briefly, 12-week-old mice were anesthetized using 1.5% inhaled isoflurane. A small
413 skin incision was made to expose the sciatic nerve at mid-thigh level, approximately 1.2 cm from
414 the L4 dorsal root ganglion (DRG). The sciatic nerve was fully crushed for 10 seconds using

415 0.1mm forceps (#55). The wound was closed with wound clips, and the mice were placed on a
416 warming pad until fully awake. At the designated time points post-surgery, L4 and L5 dorsal root
417 ganglia were dissected for further analysis. The animals were randomized into groups.

418 Dorsal root crush injuries were performed as previously described (Avraham et al., 2021).
419 Surgery was conducted on 12-week-old mice under 1.5% inhaled isoflurane anesthesia. A small
420 midline skin incision (~1 cm) was made over the thoracic vertebrae at L2-L3, followed by
421 paraspinal muscle release and stabilization of the vertebral column with metal clamps under the
422 L2-L3 transverse processes. Dorsal laminectomy was performed using forceps at the L2-L3 level,
423 and the right L3-L5 dorsal roots were crushed simultaneously for 5 seconds. The proximity
424 between L3-L5 roots resulted in a crush distance of 1-2 mm to L3 DRG, 4-5 mm to L4 DRG, and
425 7-8 mm to L5 DRG. The crushing process exerted force on the roots, causing disruption of nerve
426 fibers without interrupting the endoneurial tube. Paraspinal muscles were sutured using 6-0
427 sutures (Ethicon, Catalog#: J212H), and the wound was closed with clips. Mice were placed on a
428 warming pad until fully awake, and L4 dorsal root ganglia and L4 dorsal roots were dissected at
429 3 days post injury. The animals were randomized into groups.

430 **Drug Administration**

431 To assess the *in vivo* functions of endothelin receptors, pharmacological testing was
432 conducted. For the analysis of nerve regeneration at one day post-injury, oral gavage
433 administration of Ambrisentan (Tocris, Catalog# 5828, 10 mg/kg body weight) (Kappes et al.,
434 2020) and Bosentan (Sigma, Catalog#PHR2708, 10 mg/kg body weight) (Pinho-Ribeiro et al.,
435 2014) was performed 2 hours before the injury, with sample collection taking place 24 hours after
436 the injury. For the analysis of nerve regeneration after 3 days post-injury, Ambrisentan (10 mg/kg
437 body weight) and Bosentan (10 mg/kg body weight) were administered via oral gavage 2 hours
438 before the injury and once daily after the injury. The treatments were randomized within the
439 surgery mice group.

440 **Western Blotting**

441 L4-L5 DRGs were collected and lysed in RIPA Buffer (Cell Signaling, catalog #9806) and
442 heated at 99°C for 10 min. The protein lysates were then loaded onto an 10% Ready Gel® Tris-
443 HCl Precast Gels (BioRad, catalog#1611119) in running Buffer (BioRad, Catlog#1610744) and
444 transferred to 0.2 μm PVDF membranes (BioRad, Catalog#1620216). The membranes were
445 blocked in 5% non-fat dry milk (BioRad, Catalog#1706404XTU) Tris-Buffered Saline (TBS)
446 containing 0.1% Tween-20 at pH 7.6 for 1 h. Following blocking, the membranes were incubated
447 overnight at 4°C with Rabbit-anti-ETBR (Abcam, Catalog# ab117529, 1:1000) in blocking buffer.
448 Afterward, the membranes were washed three times with TBST (Tris-buffered saline with 0.1%
449 Tween-20), and then incubated with horseradish peroxidase-conjugated anti-rabbit (Invitrogen,
450 Catalog# 31460,1:5000) or anti-mouse (Invitrogen, Catalog # 31430,1:5000) antibodies in
451 blocking buffer for 1 h at room temperature. Subsequently, the membranes were washed three
452 times with TBST and developed using SuperSignal™ West Dura (Thermo Scientific, Catalog#
453 34075). The ChemiDoc System (Bio-Rad) was used to image the membranes. For subsequent
454 analysis, the membranes were stripped using a mild stripping buffer composed of (1.5% glycine,
455 0.1% SDS, and 1% Tween -20, pH2.2 in ddH_2O). Following stripping, the protocol was repeated
456 for GADPH staining (Santa Cruz Biotechnology, Catalog #sc-51907, 1:8000) as the loading
457 control. The resulting images were analyzed using Fiji software. To quantify the protein blots, the
458 intensity of ETBR was normalized to the intensity of GADPH. The researcher was not blinded
459 during the analysis.

460 **Quantitative real time PCR**

461 For qRT-PCR, L4 and L5 DRGs of each mouse were collected and total RNA was
462 extracted using RNeasy Mini Kit (QIAGEN, Cat# 74104). For cDNA synthesis, 500 ng of RNA
463 was converted into cDNA with the High-Capacity cDNA Reverse Transcription Kit (ThermoFisher,
464 Catalog# 4368814) according to manufacturer's specifications. Quantitative PCR was completed

465 using the PowerUp™ SYBR™ Green Master Mix (ThermoFisher, Cat# A25780) using gene-
466 specific primers (resource table) from Primerbank (https://pga.mgh.harvard.edu/primerbank/).
467 qRT-PCR was performed on a QuantStudio 6 Flex System. Expression fold change for each gene
468 of interest was calculated using the ΔCq method and normalized to the expression fold change
469 of *Gadph* expression compared to controls. The researcher was not blinded during the analysis.
470 The detail for each primer was listed in Supplementary Table 1.

471 **Immunohistochemistry**

472 Mice were euthanized with CO_2 asphyxiation and transcardially perfused with PBS
473 followed by 4% paraformaldehyde (PFA). PFA-fixed tissues were incubated in 30% sucrose in
474 phosphate-buffered saline (PBS) overnight at 4 °C, specimens were embedded in optimal cutting
475 temperature compound (OCT) (Tissue-Tek), stored at −80 °C until further processing. Transverse
476 sections of DRG (L4) and longitudinal sections of sciatic nerve were cut on a cryostat at 10μm,
477 and stored at -20 °C until processed. Before staining, sections were warmed to room temperature
478 and dried on a 60 °C slide warmer for 5 mins. Sections were treated with a blocking solution
479 containing 4% normal donkey serum (NDS) (LAMPIRE; Catalog#7332100) with 0.5% Triton X-
480 100 in PBS for 1h at room temperature. Then samples were incubated in the primary antibodies,
481 which were diluted in 1% NDS with 0.3% Triton X-100 in PBS overnight at 4°C. After three PBS
482 rinses, samples were incubated with Alexa Fluor–conjugated secondary antibodies in PBS with
483 0.3% Triton X-100 in 1h, followed by incubation in 300nM 4′,6-diamidino-2-phenylindole (DAPI,
484 Sigma-Aldrich, Catalog# D9542) at room temperature for 10 mins. Samples were rinsed before
485 mounting with ProLong™ Gold Antifade Mountant (Invitrogen, Catalog#:P36930). For co-staining
486 of Cx43 and Fabp7, both of which are rabbit antibodies, the tissue sections were first blocked with
487 10% NDS in PBS containing 0.3% Triton X-100 at room temperature for 1h. Subsequently, the
488 sections were incubated overnight at 4°C with rabbit anti-Cx43 antibody diluted in 0.1% Triton X-
489 100 in PBS. After three rinses with PBS, the samples were incubated with an excess of conjugated

490 Fab Fragment secondary antibody in PBS with 0.3% Triton X-100 for one hour. Following three
491 washes with PBS, the sections were incubated with rabbit anti-Fabp7 antibody, diluted in 0.1%
492 Triton X-100 in PBS, at room temperature for 2h. After three PBS washes, the samples were
493 incubated with Alexa Fluor-conjugated secondary antibodies in PBS with 0.3% Triton X-100 for
494 one hour. Finally, the sections were incubated with DAPI at room temperature for 10 minutes,
495 followed by rinsing and mounting with ProLong™ Gold Antifade Mountant. DRG sections were
496 imaged with a confocal laser-scanning microscope (Zeiss LSM880). Figures showing large
497 longitudinal sciatic nerve sections were produced using EVOS™ M7000 Imaging System with
498 image stitching and/or stack software. For adult DRG culture staining, neurons were fixed in pre-
499 warmed 1%PFA in 7.5% sucrose at 37 °C for 15 mins. Then post-fixed in prewarmed 2%PFA in
500 15% sucrose in 30 mins. Rise with PBS 3 times, the fixed neurons were directly for
501 immunostaining following same staining protocol described above. Cultured neurons were
502 imaged with acquired using the ECLIPSE Ti2 inverted microscope.

503 Whole-mount DRG immunostaining was performed by injecting 0.1 μL of Lycopersicon
504 Esculentum Lectin (Vector, Catalog# DL-1178-1) through the tail vein to label the blood vessels
505 (Robertson et al., 2015). L4 DRGs were dissected after 20 minutes and fixed overnight in 4% PFA
506 at 4°C. Following a previously established protocol (Yang et al., 2017), DRGs underwent a series
507 of washing and permeabilization steps with 0.3% Triton X-100 in PBS, repeated every hour for 5
508 hours. Subsequently, the tissues were incubated with primary antibodies in a blocking solution
509 consisting of 75% 0.3% PBST, 20% DMSO, and 5% Donkey Serum for 4 days, followed by further
510 washing with 0.3% Triton X-100 in PBS every hour for 5 hours. The tissues were then incubated
511 with secondary antibodies in the blocking solution for 2 days, with subsequent washing using 0.3%
512 Triton X-100 in PBS every hour for 5 hours. All of these washing and incubation procedures were
513 carried out on a rocking platform at room temperature. The tissues were dehydrated in methanol
514 for 1 hour and cleared using a 1:2 mixture of Benzyl Alcohol to Benzyl Benzoate. Imaging was

515 carried out using an LSM880 confocal microscope, and blood vessel reconstruction was
516 performed with Imaris 9.7.

517 Primary antibodies included rabbit anti-FABP7 (Invitrogen, Catalog#:PA5-24949, 1:1000);
518 rabbit anti-STMN2(SCG10) (Novus a bio-techine, Catalog#:NBP1-49461, 1:1000); rabbit anti-
519 Connexin-43 (Cell Signaling, Catalog#: 3512s, 1:200); mouse anti TUJ1 (β-III tubulin) (Biolegend,
520 Catalog#:801202, 1:1000). Secondary antibodies conjugated to Alexa Fluor 488, Alexa Fluor 594
521 and Alexa Fluor 647 (Invitrogen), conjugated Fab Fragment Donkey anti Rabbit Alexa Fluor
522 (Jackson ImmunoResearch Labs) were diluted 1:500.

523 **RNAscope® in situ hybridization**

524 The RNAscope® fluorescent multiplex reagent kit (Advanced Cell Diagnostics, ACD) was
525 used according to the manufacturer's instructions. Slides were retrieved from a -80°C freezer,
526 washed with PBS to remove OCT, and dried on a 60°C slide warmer for 5 minutes. Post-fixation
527 was performed by immersing the slides in cold (4°C) 4% paraformaldehyde (PFA) for 15 minutes.
528 Tissues were dehydrated using a series of ethanol washes (50% ethanol for 5 minutes, 70%
529 ethanol for 5 minutes, and 100% ethanol for 10 minutes) at room temperature. Slides were air
530 dried briefly and then incubated in RNAscope® Target Retrieval buffer (ACD; Catalog# 322000)
531 at 98-100°C for 5 minutes. After rinsing in 100% ethanol, hydrophobic boundaries were drawn
532 around each section using a hydrophobic pen (ImmEdge PAP pen; Vector Labs). Once the
533 boundaries were dry, protease III reagent was added to each section and incubated for 15 minutes.
534 Slides were briefly washed in PBS at room temperature. Each slide was placed in a prewarmed
535 humidity control tray (ACD) with dampened filter paper, and a mixture of probes was pipetted onto
536 each section until fully submerged. The slides were then incubated in a HybEZ oven (ACD) at
537 40°C for 2 hours. Following the probe incubation, the slides were washed twice with 1x RNAscope
538 wash buffer and returned to the oven for 30 minutes after submersion in AMP-1 reagent. This
539 washing and amplification process was repeated using AMP-2, AMP-3, and AMP-4 reagents with

540 incubation periods of 15 minutes, 30 minutes, and 15 minutes, respectively. For all mouse
541 experiments, AMP-4 ALT A (Channel 1 = Atto 488, Channel 2 = Alexa 550, Channel 3 = Atto 647)
542 was used. Slides were then washed twice with 0.1M phosphate buffer (PB, pH 7.4). Subsequently,
543 the slides were processed with 300nM DAPI at room temperature for 10 minutes and cover-
544 slipped using Prolong Gold Antifade mounting medium. DRG sections were imaged using a
545 confocal laser-scanning microscope (Zeiss LSM880).

546 **Transmission electron microscopy**

547 For transmission electron microscopy (TEM), mice were perfused PBS and then with the
548 fixative (2.5% glutaraldehyde and 4% paraformaldehyde in 0.1 M Cacodylate buffer), followed by
549 post-fixation in same fixation 24hrs at 4C. For secondary post fixation, the samples were rinsed
550 in 0.15 M cacodylate buffer containing 2mM calcium chloride 3 times for 10 minutes each followed
551 by a secondary fixation in 1% osmium tetroxide and 1.5% potassium ferrocyanide in 0.15 M
552 cacodylate buffer containing 2 mM calcium chloride for 1 hour in the dark. The samples were then
553 rinsed 3 times for 10 minutes each in ultrapure water and en bloc stained with 2% aqueous uranyl
554 acetate overnight at 4 °C in the dark. After 4 washes for 10 minutes each in ultrapure water, the
555 samples were dehydrated in a graded acetone series (10%, 30%, 50%, 70%, 90%, 100% x3) for
556 10 minutes each step, infiltrated with Spurr's resin (Electron Microscopy Sciences) and embedded
557 and polymerized at 60 °C for 72 hours. The samples from adult mice were processed as above
558 except they were dehydrated in a graded ethanol series (10%, 30%, 50%, 70%, 90%, 100% x3)
559 for 10 minutes each step, infiltrated with Epon resin (Electron Microscopy Sciences) and
560 embedded and polymerized at 60 °C for 48 hours. Post curing, 70 nm thin sections were cut,
561 post-stained with 2% aqueous uranyl acetate and Sato's lead and imaged on a TEM (Jeol JEM-
562 1400 Plus) at 120 kV.

563 **Single Cell RNA sequencing**

564 L4 and L5 DRGs from mice were collected and placed into cold dissection medium
565 consisting of Hank's Balanced Salt Solution (HBSS; ThermoFisher, Gibco; Catalog#: 14175-079)
566 supplemented with 10% 1M HEPES (ThermoFisher, Gibco; Catalog#: 15630080). Subsequently,
567 the ganglia were transferred to freshly prepared pre-warmed dissociation medium composed of
568 15 U/mL Papain suspension (Worthington Biochemical; Catalog#: LS003126), 0.3 mg/mL L-
569 cysteine (Sigma; Catalog#: C7352), 0.1 mg/mL Deoxyribonuclease I (Worthington Biochemical;
570 Catalog#: LS002139), and 10% 1M HEPES in HBSS. The samples were then incubated at 37°C
571 for 20 minutes. After two washes with pre-warmed HBSS, the ganglia were incubated with
572 collagenase (150 µg/mL; Sigma; Catalog#: C6885) at 37°C for 20 minutes. Following an additional
573 two washes with pre-warmed HBSS, the resulting single cell suspension was resuspended by
574 gently triturating in complete medium consisting of Neurobasal™-A Medium (ThermoFisher,
575 Gibco; Catalog#: 12349015) supplemented with B-27™ Plus Supplement (ThermoFisher, Gibco;
576 Catalog#: A3582801) and GlutaMAX™ Supplement (ThermoFisher, Gibco; Catalog#: 35050061).
577 The cell suspension was then passed through 70-micron cell strainers. The single cell suspension
578 was further resuspended in HBSS containing 10% 1M HEPES and 0.1% Fetal Bovine Serum
579 (FBS; ThermoFisher; Catalog#: A3160401). The cells were stained with the LIVE/DEAD™ Fixable
580 Aqua Dead Cell Stain Kit (ThermoFisher; Catalog#: L34965) to identify live cells. Live single cells
581 were sorted using the MoFlo cell sorter (Beckman Coulter, Indianapolis, IN). The sorted cells were
582 washed with a PBS+0.04% BSA solution and manually counted using a hemocytometer. The cell
583 solution was adjusted to a concentration of 700-1000 cells/µL and loaded onto the 10X Chromium
584 system.

585 Single-cell RNA-Seq libraries were prepared using the Chromium Next GEM Single Cell
586 3' (v3.1 Kit) from 10X Genomics. Read alignment and transcript counting were performed with
587 the CellRanger (v7.1.0) package from 10X Genomics and 20,584 cells with >300 genes were
588 retained for downstream analysis. Sample QC, integration, clustering, DGE, quantification, and

589 statistical analysis were performed using the Seurat package (v4.3.0). Following normalization
590 with SCTransform, anchor-based integration by sample age, and graph-based clustering, three
591 low quality and/or doublet clusters were identified and removed based on the following
592 characteristics: statistical enrichment (DGE $p < 0.05$) of mixed major cell type marker genes or
593 mitochondria-specific transcripts, low average genes per cell, and/or low average UMIs per cell.
594 After removal of low-quality samples, the remaining clusters were visualized using UMAP
595 (Uniform Manifold Approximation and Projection). Differential gene expression (DGE) analyses
596 were performed in the Seurat package with a Wilcoxon Rank Sum test, and genes with Bonferroni-
597 adjusted p-values < 0.05 were considered for downstream analysis and visualization. All cell types
598 were pooled for DEG analyses. KEGG pathway and GO enrichment were performed using the
599 clusterProfiler package in R. The researcher was not blinded during analysis.

600 **Images acquisition and quantification**

601 Confocal images were captured under the LSM880 confocal microscope (Carl Zeiss)
602 unless otherwise specified. The images were captured under following parameters: 1 × optical
603 zoom, scan speed 6, averaged 2 times, a pinhole of 1 AU, 1024 × 1024 pixel size. The z-stack
604 images were projected into overlay images using the "Maximum Intensity Projection" function in
605 Zen Black software (Carl Zeiss). Sciatic nerve longitudinal images, the spinal cord and brain
606 images were captured under the EVOS™ M7000 Imaging System (Invitrogen). The images were
607 captured under 10x objective in 1980 × 1080 pixel size. The stitched nerve images generated by
608 the EVOS imaging system. The neuronal culture images were captured under the ECLIPSE Ti2
609 inverted microscope (Nikon). The images were captured under 10x objective in 2304 × 2304 pixel
610 size. Three tissue sections were analyzed on average for each independent mouse. The
611 researcher performing this analysis was not blinded during analysis.

612 For quantifying Cx43 expression area in the DRG, the $CX43^+$ and $Fabp7^+$ area was
613 measured using "Analysis Particles" function in Fiji. To quantify CX43, confocal imaging with Z-

614 stacks (10 μm) was performed using an LSM880 microscope. The acquired images were
615 subsequently used for 3D reconstruction using Imaris 9.7 software. The staining area of FABP7
616 underwent initial surface reconstruction, while the CX43 puncta were isolated through spot
617 reconstruction at a resolution of 0.1 μm x 0.2 μm. The average number of CX43 puncta was
618 determined for each FABP7^{+} cell (Supplementary Video S1). For quantifying the regeneration
619 index in the injured sciatic nerve section, the highest SCG10 intensity along the nerve was defined
620 as the crush site, as described (Cho et al., 2013; Feng et al., 2023). The average SCG10 intensity
621 at distances away from the crush site was normalized to the SCG10 intensity at the crush site
622 using "measure" function in Fiji. For quantifying the neuron regenerative capacity in cultured DRG
623 neurons, TUJ1 stained neurons were segmented by thresholding and subjected to neurite tracing
624 using "Simple Neurite Tracer" plug-in in Fiji. The researcher was not blinded during analysis.

625 DRG explant analysis was performed by creation of an ROI around each explant. The ROI
626 was removed for organoid contrast and the radial length was measured from the outer peripheral
627 section of the ROI. The 35 longest axons in each image were measured (μm) and averaged.

628 For TEM, SGCs width around the neuron was measured by averaging 4 individual points
629 that did not contain an SGCs nucleus around the neuron using Fiji/ImageJ software. Frequency
630 of neurons with 0,1,2, or 3 SGCs nuclei per neuron was quantified by counting each image by
631 eye.

632 **Statistical analysis**

633 All statistical analyses and graphs were conducted, organized and generated in GraphPad
634 Prism 9. Numerical data were presented as mean ± SD from at least three independent animals.
635 Group mean difference was analyzed by either two-tailed unpaired Student's t-test or one-way
636 ANOVA with Bonferroni post-hoc test. For experiments including groups and multiple time-point
637 measurements, data were analyzed by two-way ANOVA with Bonferroni post-hoc test. P values
638 below 0.05 were considered as significant difference. The number of animals in each group is

presented in figure legends. No a priori exclusion criteria or statistical power calculations were used.

Data and materials availability:

All data associated with this study are presented in the paper or the Supplementary Materials. scRNA sequencing data have been deposited at NCBI Gene Expression Omnibus under accession number GSE223910 and will be publicly available upon publication.

List of Supplementary Materials

Supplementary Figures S1 to S5
Supplementary Data File S1 to S3
Supplementary Movie S1

Acknowledgments:

We would like to thank members of the Cavalli lab and the Mokalled lab for valuable discussions and suggestions. We gratefully acknowledge Michael Savio from The Alvin J. Siteman Cancer Center at Barnes-Jewish Hospital and Washington University School of Medicine for assistance with single cell sorting. We also acknowledge the assistance of John Wulf II, Gregory Strout and Dr. Sanja Sviben at the Washington University Center for Cellular Imaging (WUCCI) in electron microscopy studies, which is supported by Washington University School of Medicine, The Children's Discovery Institute of Washington University and St. Louis Children's Hospital (CDI-CORE-2015-505 and CDI-CORE-2019-813) and the Foundation for Barnes-Jewish Hospital (3770 and 4642). TEM images were acquired using an AMT Nanosprint15-MkII sCMOS camera, which was purchased with support from the Office of Research Infrastructure Programs (ORIP), a part of the NIH Office of the Director under grant (OD032186). The authors show their gratitude and respect to all animals sacrificed in this study.

Funding:

This work was funded in part by NIH grants R35 NS122260, R01 NS111719 and R21 NS115492 to V.C.

Author contributions:

R.F. and V.C. conceptualized the study, and V.C. provided study supervision. R.F., S.J. and I.A. performed experiments and analyzed data. R.F., S.F.R, S.J. and I.A. generated figures and visualizations. M.B.T performed bioinformatics analyses. C.G and V.C. provided study supervision. R.F., S.F.R and V.C. wrote the manuscript and all authors edited the manuscript.

Competing interests:

Washington University in St Louis has filed a provisional patent application with the US Patent and Trademark Office on this work.

675 **FIGURES LEGENDS**
676
677 **Fig. 1 *Ednrb* is highly expressed in satellite glial cells.**
678 **A.** Representative whole-mount stained images of DRG from Lycopersicon Esculentum Lectin
679 (LEL) injected Fabp7CreER::Ai14 mice, labeled for TUJ1 (green), tdTomato (magenta), and LEL
680 (grey). 3D reconstruction of blood vessels via LEL labeling (scale bars, 200 μm)**.**
681 **B.** Representative z-stack images of sectioned DRG from Lycopersicon Esculentum Lectin (LEL)
682 injected C57BL/6 mice, labeled for TUJ1 (green), Fabp7 (red), and LEL (cyan) (Scale bars, 100
683 μm).
684 **C.** UMAP analysis identified 7 cell clusters based on known marker genes.
685 **D.** Differential gene expression analysis revealed up- and down-regulated genes across cell
686 clusters. Red or green indicates adjusted $p < 0.01$, while gray indicates $p \geq 0.01$.
687 **E-F.** UMAP overlay for expression of *Ednra* (**E**) and *Ednrb* (**F**).
688 **G**. Dot plot analysis showing the average gene expression (color coded) and number of
689 expressing cells (dot size) for the marker genes.
690 **H.** Representative RNAScope *in situ* hybridization images showing *Ednrb* (red), *Fabp7* (cyan) and
691 DAPI (blue) of L4 DRGs from 3-month-old mice (scale bars, 50 μm).
692
693 **Fig. 2 Endothelin B receptor inhibition increases axonal growth *in vitro* and *ex vivo.***
694 **A.** Representative images showing TUJ1 (black) immunostaining of neurons in DRG cultures
695 (scale bars, 100 μm).
696 **B-C.** Quantification of axonal radial length (B) and $TUJ1^+$ area (C) per neuron. Different colors
697 indicate biological replicates. N = 246 (Veh; 8 replicates), 318 (BQ788; 8 replicates), 320 (IRL1620;
698 8 replicates), and 244 (BQ123; 8 replicates). Data presented as mean ± SD.
699 **D.** Scheme of drug treatment and DRG explant model.
700 **E.** Representative images of DRG explants 7 days after drug treatment, immunostained for
701 TUJ1 (black) (scale bars, 1000 μm).
702 **F.** Quantification of radial length of the 35 longest axons from DRG explants from indicated
703 groups N=36 (BQ788; 18 replicates, Veh; 18 replicates).
704 **G.** Representative images of DRG explants immunostained for TUJ1 (green), FABP7 (magenta),
705 and merged (scale bars, 50 μm).
706
707 **Fig. 3 Bosentan treatment improves axonal regeneration after peripheral nerve injury in**
708 **adult mice.**
709 **A.** Scheme of drug treatment and peripheral nerve injury model.
710 **B.** Quantification of the length of the 10 longest axons in indicated conditions.
711 **C**. Quantification of the regeneration index, calculated as the distance along the nerve where
712 the SGC10 intensity is 50% of the SCG10 intensity at crush site.
713 **D.** Representative longitudinal sections of sciatic nerves 24h after SNC, immunostained for
714 SCG10, from mice with the indicated treatment. Dotted line indicates the crush site, determined
715 as the maximal SGC10 intensity (scale bars, 200 μm).
716 **E.** Quantificaiton of SCG10 intensity at the indicated distance normalized to the intensity at the
717 crush site for each condition. N = 5 mice/condition.
718 **F**. Scheme of adult DRG neuronal culture and treatments.
719 **G.** Representative images showing TUJ1 (black) immunostaining of neurons in DRG cultures
720 (scale bars, 100 μm).
721 **H-I.** Quantification of axonal radial length (K) and total $TUJ1^+$ area (L). Different colors represent
722 different biological replicates. N (neuron number) = 177 (vehicle; three biological replicates,
723 naïve mice), 168 (Ambrisentan, three biological replicates, naïve mice), 183 (Bosentan; three
724 biological replicates, naïve mice), 186 (vehicle; three biological replicates, injured mice),

204(Ambrisentan, three biological replicates, injured mice) and 210 (Bosentan; three biological replicates, injured mice), respectively. The data are presented as mean ± SD.

Fig. 4 Bosentan treatment rescues aging-dependent neuronal regenerative decline.
A. Scheme of drug treatment and DRG explant model.
B. Representative images of DRG explants 7 days after drug treatment (scale bars, 1000 μm).
C. Quantification of radial length of the 50 longest axons from DRG explants. N=36 (BQ788; 18 replicates, Veh; 18 replicates).
D. Representative longitudinal sections of sciatic nerves 3 d after SNC immunostained for SCG10 from mice with the indicated treatment. Dotted line indicates the crush site, determined as the maximal SCG10 intensity (scale bars, 200 μm).
E-F. Quantification of the 10 longest axons in indicated groups (**E**). Quantificaiton of 50% regenerative index, calculated as the disatnce along the nerve where the SCG10 intensity is 50% of the SCG10 intensity at crush site (**F**).
G. Quantification of the SCG10 intensity at the indicated distance normalized to the intensity at the crush site for each condition. N (mouse number) = 4(adult, vehicle), 3 (Aged, vehicle) and 3 (Bosentan+Age), respectively. The data are presented as mean ± SD.

Fig. 5 ETBR inhibition increases the expression of Cx43 in SGCs in adult and aged mice.
A. UMAP overlay for expression of *Gja1* in mouse DRG.
B. Box and whisker plot of *Gja1* gene expression in 5 donors, each dot represents a single cell.
C. Plot showing the average gene expression of *Gja1, Gjb2, Gjb6 and Gjc1* genes in SGCs in adult (2M), mid-aged (12M), and aged (21M) mice.
D. Scheme of drug treatment and peripheral nerve injury model.
E. Quantification of the percentage of the Cx43/FABP7 expression area.
F. Quantification of the average number of Connexin 43 (Cx43) puncta per FABP7+ cell. The ratio of total Cx43 puncta to the number of FABP7+ cells surrounding a TUJ1+ neuron was measured. N(cell number) = 60(adult, uninjured), 62(aged, uninjured), 96(vehicle, adult, SNC), 117(bosentan, adult, SNC), 74(vehicle, aged, SNC) and 74(bosentan, aged, SNC), respectively.
G. Representative immunostaining images showing Connexin 43 (Cx43), FABP7 and TUJ1 in L4 DRGs from the indicated condition (scale bars, 50 μm).

Fig. 6 Aging alters SGCs morphology and metabolism.
A. Representative TEM images of DRG sections from adult (2M), middle aged (12M) and aged (21M) mice showing neuronal cell bodies and the enveloping SGCs (SGCs are pseudo-colored in red) (scale bars, 5 μm).
B. Quantification of the average width of SGCs per neuron in μms.
C. Frequency of neurons with 0, 1, 2, or 3 SGC nuclei per neuron in TEM images for 2M, 12M, and 21M old mice.
D. UMAP analysis of 6430 SGCs from mice of different age.
E-F. Venn diagrams were constructed to compare the sets of differentially expressed genes (DEGs) that were upregulated (**E**) and downregulated (**F**) in the mid-aged vs. adult comparison and in aged vs. adult. (FDR $\leqslant$ 0.05, fold-change $\geqslant$ 2).
G-H. KEGG analysis was performed on the common upregulated DEGs (**G**) and common downregulated DEGs (**H**). The dots in the diagram represent the count of genes associated with each pathway.

SUPPLEMENTARY FIGURES

Supp Fig. 1

A. UMAP plots of genes used for cell cluster annotations.
B. Plot of the average gene expression changes of *Edn1*, *Edn3*, and *Ednrb* in adult, mid-age and aged mice.
C. Box and whisker plot of *Ednrb* expression in the indicated cell types in rat DRG.
D. Box and whisker plot of *Ednrb* gene expression in 5 human donors, each dot represents a single cell.

Supp Fig. 2

A. Scheme of drug treatment and peripheral nerve injury model.
B. Quantification of the 10 longest axons in indicated groups.
C. Quantificaiton of 50% regenerative index, calculated as the disatnce along the nerve where the SCG10 intensity is 50% of the SCG10 intensity at crush site.
D. Representative longitudinal sections of sciatic nerves 3 d after SNC immunostained for SCG10 from mice with the indicated treatment. Dotted line indicates the crush site, determined as the maximal SCG10 intensity (scale bars, 200 μm).
E. Quantificaiton of SCG10 intensity at the indicated distance normalized to the intensity at the crush site for each condition. N = 5 mice/condition. The data are presented as mean ± SD.
F. RT-qPCR of *Atf3, Aif1, Fabp7, Edn1, Ednra* and *Ednrb* gene in contralateral (CON) and ipsilateral DRGs at 3days post injury(SNC). N (mouse number) = 4/each group.
G. Western blot analysis and quantification of ETBR protein expression in DRGs from the mice with/without injury.
H. Quantification of ETBR expression normalized to GAPDH expression (folder of control mice). N (mouse number) = 8/group. The data are presented as mean ± SD.

Supp Fig. 3

A. Scheme of drug treatment and dorsal root crush injury model.
B. Representative longitudinal sections of sciatic nerves 3 d after DRC immunostained for SCG10 from mice with the indicated treatment. Dotted line indicates the crush site, determined as the maximal SCG10 intensity (scale bars, 200 μm).
C. Quantification of the 10 longest axons in indicated groups.
D. Quantificaiton of 50% regenerative index, calculated as the disatnce along the nerve where the SCG10 intensity is 50% of the SCG10 intensity at crush site.
E. Quantificaiton of SCG10 intensity at the indicated distance normalized to the intensity at the crush site for each condition. N = 5 mice/condition. The data are presented as mean ± SD.

Supp Fig. 4

A. Representative immunostaining images of connexin 43 (red), Fabp7 (gray), and TUJ1 (cyan) in L4 DRGs from mice of the indicated ages and treatments 3 d after dorsal root crush injury (scale bars, 50 μm).
B. Quantification of the percentage of the Cx43/FABP7 expression area in each condition.
C. Quantification of the average number of Connexin 43 (Cx43) puncta per $FABP7^+$ cell. The ratio of total Cx43 puncta to the number of $FABP7^+$ cells surrounding a TUJ1-positive neuron was measured.Different colors were used to indicate distinct biological replicates (mouse). N(cell number) = 93 (uninjured), 97 (Vehicle, DRC), and 124 (Bosentan, DRC), respectively. The data are presented as mean ± SD.

827 **Supp Fig. 5**
828 **A.** Volcano plot of upregulated and downregulated genes in mid-aged vs. adult, aged vs. adult,
829 and aged vs. mid-aged.
830 **B.** Gene ontology analysis of upregulated and downregulated genes from all cells overlapping in
831 mid-aged or aged groups compared to adults.
832
833
834
835

836 **REFERENCES**

837 Andrews, M.R., Soleman, S., Cheah, M., Tumbarello, D.A., Mason, M.R., Moloney, E., Verhaagen,
838 J., Bensadoun, J.C., Schneider, B., Aebischer, P.*, et al.* (2016). Axonal Localization of Integrins
839 in the CNS Is Neuronal Type and Age Dependent. eNeuro *3*.

840 Avraham, O., Chamessian, A., Feng, R., Yang, L., Halevi, A.E., Moore, A.M., Gereau, R.W.t., and
841 Cavalli, V. (2022). Profiling the molecular signature of satellite glial cells at the single cell level
842 reveals high similarities between rodents and humans. Pain *163*, 2348-2364.

843 Avraham, O., Deng, P.Y., Jones, S., Kuruvilla, R., Semenkovich, C.F., Klyachko, V.A., and Cavalli,
844 V. (2020). Satellite glial cells promote regenerative growth in sensory neurons. Nat Commun *11*,
845 4891.

846 Avraham, O., Feng, R., Ewan, E.E., Rustenhoven, J., Zhao, G., and Cavalli, V. (2021). Profiling
847 sensory neuron microenvironment after peripheral and central axon injury reveals key pathways
848 for neural repair. Elife *10*.

849 Barton, M. (2014). Aging and endothelin: determinants of disease. Life Sci *118*, 97-109.

850 Black, M.M., and Lasek, R.J. (1979). Slowing of the rate of axonal regeneration during growth
851 and maturation. Experimental neurology *63*, 108-119.

852 Blomstrand, F., Venance, L., Siren, A.L., Ezan, P., Hanse, E., Glowinski, J., Ehrenreich, H., and
853 Giaume, C. (2004). Endothelins regulate astrocyte gap junctions in rat hippocampal slices. The
854 European journal of neuroscience *19*, 1005-1015.

855 Brennan, A., Dean, C.H., Zhang, A.L., Cass, D.T., Mirsky, R., and Jessen, K.R. (2000).
856 Endothelins control the timing of Schwann cell generation in vitro and in vivo. Developmental
857 biology *227*, 545-557.

858 Buttner, R., Schulz, A., Reuter, M., Akula, A.K., Mindos, T., Carlstedt, A., Riecken, L.B., Baader,
859 S.L., Bauer, R., and Morrison, H. (2018). Inflammaging impairs peripheral nerve maintenance and
860 regeneration. Aging Cell *17*, e12833.

861 Carlin, D., Halevi, A.E., Ewan, E.E., Moore, A.M., and Cavalli, V. (2019). Nociceptor Deletion of
862 Tsc2 Enhances Axon Regeneration by Inducing a Conditioning Injury Response in Dorsal Root
863 Ganglia. eNeuro *6*.

864 Chen, X., Zhai, Z., Huang, K., Xie, W., Wan, J., and Wang, C. (2018). Bosentan therapy for
865 pulmonary arterial hypertension and chronic thromboembolic pulmonary hypertension: A
866 systemic review and meta-analysis. Clin Respir J *12*, 2065-2074.

867 Cho, Y., and Cavalli, V. (2012). HDAC5 is a novel injury-regulated tubulin deacetylase controlling
868 axon regeneration. EMBO J *31*, 3063-3078.

869 Cho, Y., Shin, J.E., Ewan, E.E., Oh, Y.M., Pita-Thomas, W., and Cavalli, V. (2015). Activating
870 Injury-Responsive Genes with Hypoxia Enhances Axon Regeneration through Neuronal HIF-
871 1alpha. Neuron *88*, 720-734.

872 Cho, Y., Sloutsky, R., Naegle, K.M., and Cavalli, V. (2013). Injury-induced HDAC5 nuclear export
873 is essential for axon regeneration. Cell *155*, 894-908.

874 Clozel, M., Breu, V., Gray, G.A., Kalina, B., Loffler, B.M., Burri, K., Cassal, J.M., Hirth, G., Muller,
875 M., Neidhart, W.*, et al.* (1994). Pharmacological characterization of bosentan, a new potent orally
876 active nonpeptide endothelin receptor antagonist. J Pharmacol Exp Ther *270*, 228-235.

877 Cotrina, M.L., Lin, J.H., and Nedergaard, M. (2008). Adhesive properties of connexin
878 hemichannels. Glia *56*, 1791-1798.

879 Feldman-Goriachnik, R., and Hanani, M. (2017). The effects of endothelin-1 on satellite glial cells
880 in peripheral ganglia. Neuropeptides *63*, 37-42.

881 Feng, R., Muraleedharan Saraswathy, V., Mokalled, M.H., and Cavalli, V. (2023). Self-renewing
882 macrophages in dorsal root ganglia contribute to promote nerve regeneration. Proceedings of the
883 National Academy of Sciences of the United States of America *120*, e2215906120.

884 Fuentes-Flores, A., Geronimo-Olvera, C., Girardi, K., Necunir-Ibarra, D., Patel, S.K., Bons, J.,
885 Wright, M.C., Geschwind, D., Hoke, A., Gomez-Sanchez, J.A.*, et al.* (2023). Senescent Schwann
886 cells induced by aging and chronic denervation impair axonal regeneration following peripheral
887 nerve injury. EMBO Mol Med *15*, e17907.

888 Galie, N., Olschewski, H., Oudiz, R.J., Torres, F., Frost, A., Ghofrani, H.A., Badesch, D.B.,
889 McGoon, M.D., McLaughlin, V.V., Roecker, E.B.*, et al.* (2008). Ambrisentan for the treatment of
890 pulmonary arterial hypertension: results of the ambrisentan in pulmonary arterial hypertension,
891 randomized, double-blind, placebo-controlled, multicenter, efficacy (ARIES) study 1 and 2.
892 Circulation *117*, 3010-3019.

893 Geoffroy, C.G., Hilton, B.J., Tetzlaff, W., and Zheng, B. (2016). Evidence for an Age-Dependent
894 Decline in Axon Regeneration in the Adult Mammalian Central Nervous System. Cell reports *15*,
895 238-246.

896 Geoffroy, C.G., Meves, J.M., and Zheng, B. (2017). The age factor in axonal repair after spinal
897 cord injury: A focus on neuron-intrinsic mechanisms. Neuroscience letters *652*, 41-49.

898 Giaid, A., Gibson, S.J., Ibrahim, B.N., Legon, S., Bloom, S.R., Yanagisawa, M., Masaki, T.,
899 Varndell, I.M., and Polak, J.M. (1989). Endothelin 1, an endothelium-derived peptide, is expressed
900 in neurons of the human spinal cord and dorsal root ganglia. Proceedings of the National
901 Academy of Sciences of the United States of America *86*, 7634-7638.

902 Godel, T., Pham, M., Heiland, S., Bendszus, M., and Baumer, P. (2016). Human dorsal-root-
903 ganglion perfusion measured in-vivo by MRI. Neuroimage *141*, 81-87.

904 Hanani, M., Huang, T.Y., Cherkas, P.S., Ledda, M., and Pannese, E. (2002). Glial cell plasticity
905 in sensory ganglia induced by nerve damage. Neuroscience *114*, 279-283.

906 Hanani, M., and Spray, D.C. (2020). Emerging importance of satellite glia in nervous system
907 function and dysfunction. Nat Rev Neurosci *21*, 485-498.

908 Hanani, M., and Verkhratsky, A. (2021). Satellite Glial Cells and Astrocytes, a Comparative
909 Review. Neurochem Res.

910 He, Z., and Jin, Y. (2016). Intrinsic Control of Axon Regeneration. Neuron *90*, 437-451.

911 Hoke, A. (2006). Mechanisms of Disease: what factors limit the success of peripheral nerve
912 regeneration in humans? Nat Clin Pract Neurol *2*, 448-454.

913 Huang, T.Y., Cherkas, P.S., Rosenthal, D.W., and Hanani, M. (2005). Dye coupling among
914 satellite glial cells in mammalian dorsal root ganglia. Brain research *1036*, 42-49.

915 Huang, T.Y., Hanani, M., Ledda, M., De Palo, S., and Pannese, E. (2006). Aging is associated
916 with an increase in dye coupling and in gap junction number in satellite glial cells of murine dorsal
917 root ganglia. Neuroscience *137*, 1185-1192.

918 Humbert, M., Sitbon, O., and Simonneau, G. (2004). Treatment of pulmonary arterial hypertension.
919 N Engl J Med *351*, 1425-1436.

920 Jager, S.E., Pallesen, L.T., Richner, M., Harley, P., Hore, Z., McMahon, S., Denk, F., and Vaegter,
921 C.B. (2020). Changes in the transcriptional fingerprint of satellite glial cells following peripheral
922 nerve injury. Glia.

923 Jankowich, M., and Choudhary, G. (2020). Endothelin-1 levels and cardiovascular events. Trends
924 Cardiovasc Med *30*, 1-8.

925 Jessen, K.R., and Mirsky, R. (2016). The repair Schwann cell and its function in regenerating
926 nerves. J Physiol *594*, 3521-3531.

927 Jimenez-Andrade, J.M., Herrera, M.B., Ghilardi, J.R., Vardanyan, M., Melemedjian, O.K., and
928 Mantyh, P.W. (2008). Vascularization of the dorsal root ganglia and peripheral nerve of the mouse:
929 implications for chemical-induced peripheral sensory neuropathies. Molecular pain *4*, 10.

930 Kang, H., and Lichtman, J.W. (2013). Motor axon regeneration and muscle reinnervation in young
931 adult and aged animals. The Journal of neuroscience : the official journal of the Society for
932 Neuroscience *33*, 19480-19491.

933 Kappes, L., Amer, R.L., Sommerlatte, S., Bashir, G., Plattfaut, C., Gieseler, F., Gemoll, T., Busch,
934 H., Altahrawi, A., Al-Sbiei, A.*, et al.* (2020). Ambrisentan, an endothelin receptor type A-selective
935 antagonist, inhibits cancer cell migration, invasion, and metastasis. Scientific reports *10*, 15931.

936 Khodorova, A., Montmayeur, J.P., and Strichartz, G. (2009). Endothelin receptors and pain. The
937 journal of pain : official journal of the American Pain Society *10*, 4-28.

938 Kim, Y.S., Anderson, M., Park, K., Zheng, Q., Agarwal, A., Gong, C., Saijilafu, Young, L., He, S.,
939 LaVinka, P.C.*, et al.* (2016). Coupled Activation of Primary Sensory Neurons Contributes to
940 Chronic Pain. Neuron *91*, 1085-1096.

941 Li, S., Overman, J.J., Katsman, D., Kozlov, S.V., Donnelly, C.J., Twiss, J.L., Giger, R.J., Coppola,
942 G., Geschwind, D.H., and Carmichael, S.T. (2010). An age-related sprouting transcriptome
943 provides molecular control of axonal sprouting after stroke. Nature neuroscience *13*, 1496-1504.

944 Luscher, T.F., and Barton, M. (2000). Endothelins and endothelin receptor antagonists:
945 therapeutic considerations for a novel class of cardiovascular drugs. Circulation *102*, 2434-2440.

946 Madisen, L., Zwingman, T.A., Sunkin, S.M., Oh, S.W., Zariwala, H.A., Gu, H., Ng, L.L., Palmiter,
947 R.D., Hawrylycz, M.J., Jones, A.R.*, et al.* (2010). A robust and high-throughput Cre reporting and
948 characterization system for the whole mouse brain. Nature neuroscience *13*, 133-140.

949 Mahar, M., and Cavalli, V. (2018). Intrinsic mechanisms of neuronal axon regeneration. Nat Rev
950 Neurosci *19*, 323-337.

951 Maita, K.C., Garcia, J.P., Avila, F.R., Torres-Guzman, R.A., Ho, O., Chini, C.C.S., Chini, E.N.,
952 and Forte, A.J. (2023). Evaluation of the Aging Effect on Peripheral Nerve Regeneration: A
953 Systematic Review. J Surg Res *288*, 329-340.

954 Mapps, A.A., Thomsen, M.B., Boehm, E., Zhao, H., Hattar, S., and Kuruvilla, R. (2022). Diversity
955 of satellite glia in sympathetic and sensory ganglia. Cell reports *38*, 110328.

956 Maruoka, H., Kubota, K., Kurokawa, R., Tsuruno, S., and Hosoya, T. (2011). Periodic organization
957 of a major subtype of pyramidal neurons in neocortical layer V. The Journal of neuroscience : the
958 official journal of the Society for Neuroscience *31*, 18522-18542.

959 Mazaud, D., Capano, A., and Rouach, N. (2021). The many ways astroglial connexins regulate
960 neurotransmission and behavior. Glia *69*, 2527-2545.

961 Nagashima, K., and Oota, K. (1974). A histopathological study of the human spinal ganglia. 1.
962 Normal variations in aging. Acta Pathol Jpn *24*, 333-344.

963 Newman, J.H., Kar, S., and Kirkpatrick, P. (2007). Ambrisentan. Nat Rev Drug Discov *6*, 697-698.

964 Oblinger, M.M., and Lasek, R.J. (1984). A conditioning lesion of the peripheral axons of dorsal
965 root ganglion cells accelerates regeneration of only their peripheral axons. The Journal of
966 neuroscience : the official journal of the Society for Neuroscience *4*, 1736-1744.

967 Ohara, P.T., Vit, J.P., Bhargava, A., and Jasmin, L. (2008). Evidence for a role of connexin 43 in
968 trigeminal pain using RNA interference in vivo. J Neurophysiol *100*, 3064-3073.

969 Painter, M.W., Brosius Lutz, A., Cheng, Y.C., Latremoliere, A., Duong, K., Miller, C.M., Posada,
970 S., Cobos, E.J., Zhang, A.X., Wagers, A.J.*, et al.* (2014). Diminished Schwann cell repair
971 responses underlie age-associated impaired axonal regeneration. Neuron *83*, 331-343.

972 Pannese, E. (1981). The satellite cells of the sensory ganglia. Advances in anatomy, embryology,
973 and cell biology *65*, 1-111.

974 Pannese, E. (2010). The structure of the perineuronal sheath of satellite glial cells (SGCs) in
975 sensory ganglia. Neuron glia biology *6*, 3-10.

976 Pannese, E., Ledda, M., Cherkas, P.S., Huang, T.Y., and Hanani, M. (2003). Satellite cell
977 reactions to axon injury of sensory ganglion neurons: increase in number of gap junctions and
978 formation of bridges connecting previously separate perineuronal sheaths. Anatomy and
979 embryology *206*, 337-347.

980 Pannese, E., Ledda, M., Martinelli, C., and Sartori, P. (1997). Age-related decrease of the
981 perineuronal satellite cell number in the rabbit spinal ganglia. J Peripher Nerv Syst *2*, 77-81.

982 Pannese, E., Procacci, P., Ledda, M., and Conte, V. (1996). Age-related reduction of the satellite
983 cell sheath around spinal ganglion neurons in the rabbit. J Neurocytol *25*, 137-146.

984 Peacock, A.J., Zamboni, W., and Vizza, C.D. (2015). Ambrisentan for the treatment of adults with
985 pulmonary arterial hypertension: a review. Curr Med Res Opin *31*, 1793-1807.

986 Pestronk, A., Drachman, D.B., and Griffin, J.W. (1980). Effects of aging on nerve sprouting and
987 regeneration. Experimental neurology *70*, 65-82.

988 Pinho-Ribeiro, F.A., Borghi, S.M., Staurengo-Ferrari, L., Filgueiras, G.B., Estanislau, C., and Verri,
989 W.A., Jr. (2014). Bosentan, a mixed endothelin receptor antagonist, induces antidepressant-like
990 activity in mice. Neuroscience letters *560*, 57-61.

991 Pomonis, J.D., Rogers, S.D., Peters, C.M., Ghilardi, J.R., and Mantyh, P.W. (2001). Expression
992 and localization of endothelin receptors: implications for the involvement of peripheral glia in
993 nociception. The Journal of neuroscience : the official journal of the Society for Neuroscience *21*,
994 999-1006.

995 Procacci, P., Magnaghi, V., and Pannese, E. (2008). Perineuronal satellite cells in mouse spinal
996 ganglia express the gap junction protein connexin43 throughout life with decline in old age. Brain
997 research bulletin *75*, 562-569.

998 Quist, A.P., Rhee, S.K., Lin, H., and Lal, R. (2000). Physiological role of gap-junctional
999 hemichannels. Extracellular calcium-dependent isosmotic volume regulation. The Journal of cell
1000 biology *148*, 1063-1074.

1001 Retamal, M.A., Riquelme, M.A., Stehberg, J., and Alcayaga, J. (2017). Connexin43 Hemichannels
1002 in Satellite Glial Cells, Can They Influence Sensory Neuron Activity? Front Mol Neurosci *10*, 374.

1003 Rishal, I., and Fainzilber, M. (2014). Axon-soma communication in neuronal injury. Nat Rev
1004 Neurosci *15*, 32-42.

1005 Robertson, R.T., Levine, S.T., Haynes, S.M., Gutierrez, P., Baratta, J.L., Tan, Z., and Longmuir,
1006 K.J. (2015). Use of labeled tomato lectin for imaging vasculature structures. Histochem Cell Biol
1007 *143*, 225-234.

1008 Rozyczka, J., Figiel, M., and Engele, J. (2005). Chronic endothelin exposure inhibits connexin43
1009 expression in cultured cortical astroglia. J Neurosci Res *79*, 303-309.

1010 Rubin, L.J., Badesch, D.B., Barst, R.J., Galie, N., Black, C.M., Keogh, A., Pulido, T., Frost, A.,
1011 Roux, S., Leconte, I.*, et al.* (2002). Bosentan therapy for pulmonary arterial hypertension. N Engl
1012 J Med *346*, 896-903.

1013 Shin, J.E., Geisler, S., and DiAntonio, A. (2014). Dynamic regulation of SCG10 in regenerating
1014 axons after injury. Experimental neurology *252*, 1-11.

1015 Smith, D.S., and Skene, J.H. (1997). A transcription-dependent switch controls competence of
1016 adult neurons for distinct modes of axon growth. The Journal of neuroscience : the official journal
1017 of the Society for Neuroscience *17*, 646-658.

1018 Stauffer, B.L., Westby, C.M., and DeSouza, C.A. (2008). Endothelin-1, aging and hypertension.
1019 Curr Opin Cardiol *23*, 350-355.

1020 Sutherland, T.C., Sefiani, A., Horvat, D., Huntington, T.E., Lei, Y., West, A.P., and Geoffroy, C.G.
1021 (2021). Age-Dependent Decline in Neuron Growth Potential and Mitochondria Functions in
1022 Cortical Neurons. Cells *10*.

1023 Tasdemir-Yilmaz, O.E., Druckenbrod, N.R., Olukoya, O.O., Dong, W., Yung, A.R., Bastille, I.,
1024 Pazyra-Murphy, M.F., Sitko, A.A., Hale, E.B., Vigneau, S.*, et al.* (2021). Diversity of developing
1025 peripheral glia revealed by single-cell RNA sequencing. Dev Cell *56*, 2516-2535 e2518.

1026 Tedeschi, A., and Bradke, F. (2017). Spatial and temporal arrangement of neuronal intrinsic and
1027 extrinsic mechanisms controlling axon regeneration. Current opinion in neurobiology *42*, 118-127.

1028 Vaughan, D.W. (1992). Effects of advancing age on peripheral nerve regeneration. The Journal
1029 of comparative neurology *323*, 219-237.

1030 Verdu, E., Ceballos, D., Vilches, J.J., and Navarro, X. (2000). Influence of aging on peripheral
1031 nerve function and regeneration. J Peripher Nerv Syst *5*, 191-208.

1032 Wujek, J.R., and Lasek, R.J. (1983). Correlation of axonal regeneration and slow component B in
1033 two branches of a single axon. The Journal of neuroscience : the official journal of the Society for
1034 Neuroscience *3*, 243-251.

1035 Yanagisawa, M., Kurihara, H., Kimura, S., Tomobe, Y., Kobayashi, M., Mitsui, Y., Yazaki, Y., Goto,
1036 K., and Masaki, T. (1988). A novel potent vasoconstrictor peptide produced by vascular
1037 endothelial cells. Nature *332*, 411-415.

1038 Yang, L., Dong, F., Yang, Q., Yang, P.F., Wu, R., Wu, Q.F., Wu, D., Li, C.L., Zhong, Y.Q., Lu,
1039 Y.J.*, et al.* (2017). FGF13 Selectively Regulates Heat Nociception by Interacting with Na(v)1.7.
1040 Neuron *93*, 806-821 e809.

1041 Ydens, E., Amann, L., Asselbergh, B., Scott, C.L., Martens, L., Sichien, D., Mossad, O., Blank, T.,
1042 De Prijck, S., Low, D.*, et al.* (2020). Profiling peripheral nerve macrophages reveals two
1043 macrophage subsets with distinct localization, transcriptome and response to injury. Nature
1044 neuroscience *23*, 676-689.

1045 Yun, M.H. (2015). Changes in Regenerative Capacity through Lifespan. Int J Mol Sci *16*, 25392-
1046 25432.

1047 Zhou, L., Kong, G., Palmisano, I., Cencioni, M.T., Danzi, M., De Virgiliis, F., Chadwick, J.S.,
1048 Crawford, G., Yu, Z., De Winter, F.*, et al.* (2022). Reversible CD8 T cell-neuron cross-talk causes
1049 aging-dependent neuronal regenerative decline. Science *376*, eabd5926.

1050 Zigmond, R.E., and Echevarria, F.D. (2019). Macrophage biology in the peripheral nervous
1051 system after injury. Prog Neurobiol *173*, 102-121.

1052

Fig.1

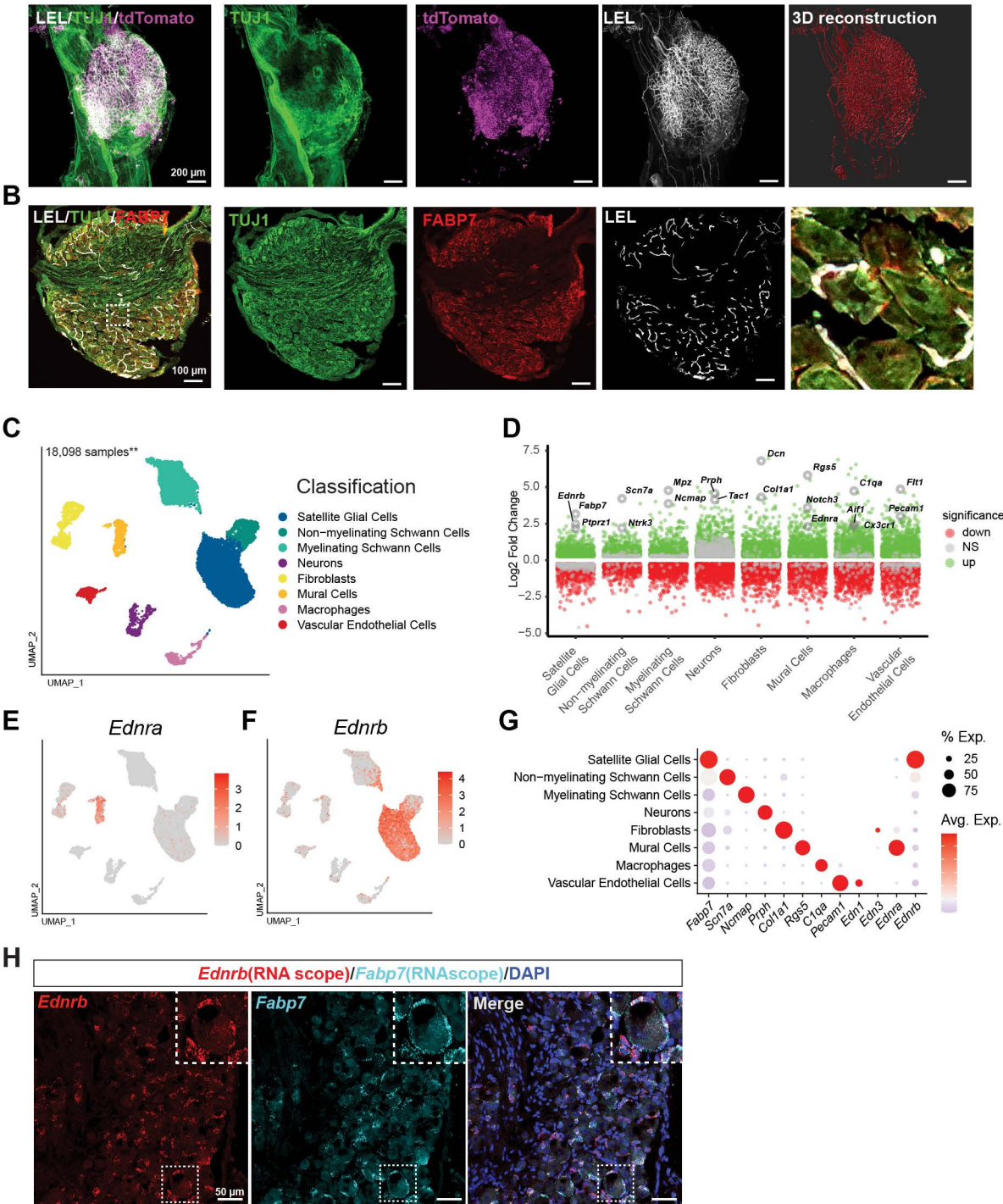
A
LEL/TUJ1/tdTomato
200 μm
TUJ1
tdTomato
LEL
3D reconstruction
B
LEL/TUJ1/FABP7
100 μm
TUJ1
FABP7
LEL
C
18,098 samples**
Classification
Satellite Glial Cells
Non−myelinating Schwann Cells
Myelinating Schwann Cells
Neurons
Fibroblasts
Mural Cells
Macrophages
Vascular Endothelial Cells
UMAP_2
UMAP_1
D
Log2 Fold Change
significance
down
NS
up
Dcn
Rgs5
Ednrb
Fabp7
Ptprz1
Scn7a
Ntrk3
Mpz
Ncmap
Prph
Tac1
Col1a1
Notch3
Ednra
C1qa
Aif1
Cx3cr1
Flt1
Pecam1
Satellite Glial Cells
Non−myelinating Schwann Cells
Myelinating Schwann Cells
Neurons
Fibroblasts
Mural Cells
Macrophages
Vascular Endothelial Cells
E
Ednra
F
Ednrb
G
% Exp.
Avg. Exp.
Satellite Glial Cells
Non−myelinating Schwann Cells
Myelinating Schwann Cells
Neurons
Fibroblasts
Mural Cells
Macrophages
Vascular Endothelial Cells
Fabp7
Scn7a
Nomap
Prph
Col1a1
Rgs5
C1qa
Pecam1
Edn1
Edn3
Ednra
Ednrb
H
Ednrb(RNA scope)/Fabp7(RNAscope)/DAPI
Ednrb
Fabp7
Merge
50 μm

Fig. 2

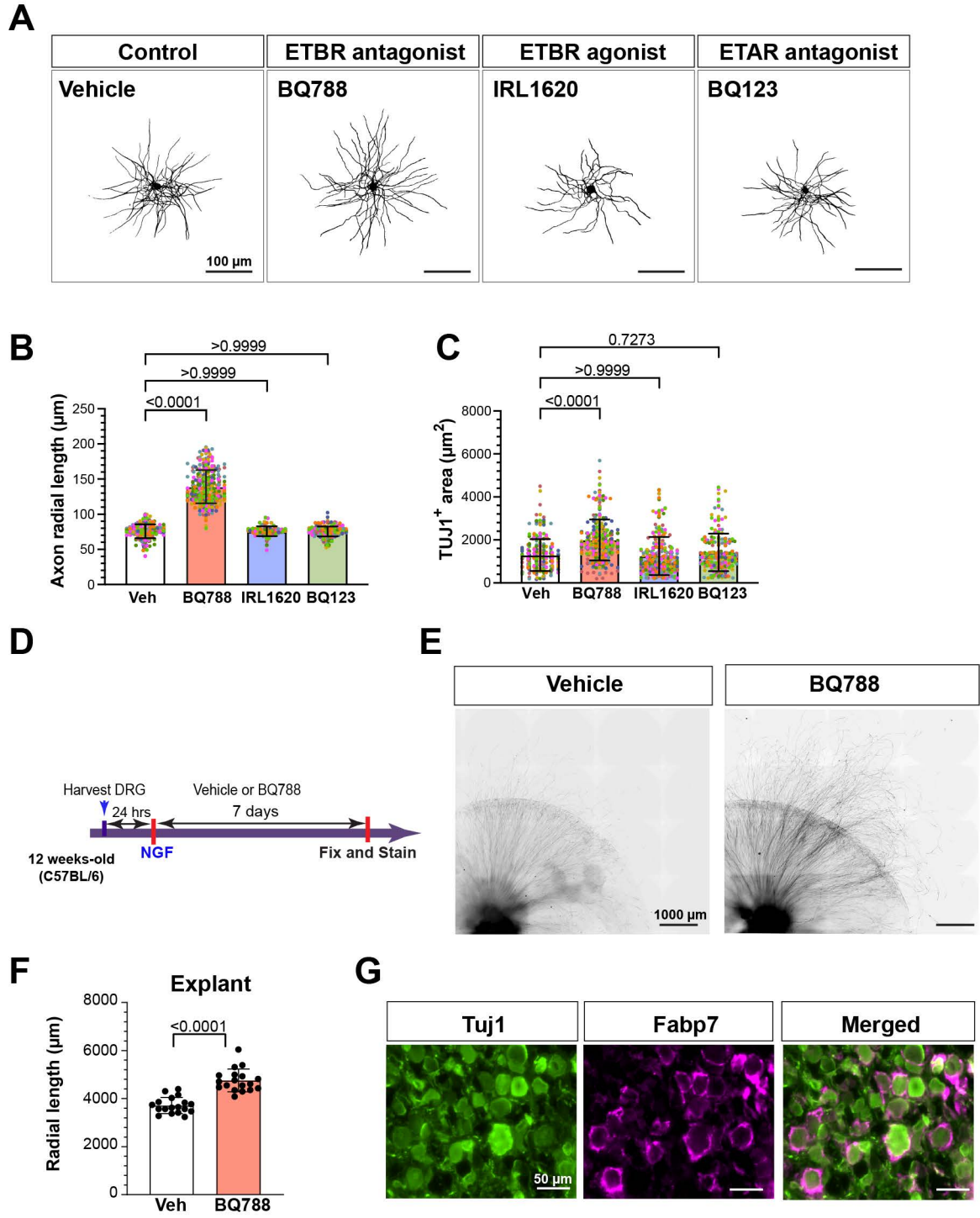
A
Control
ETBR antagonist
ETBR agonist
ETAR antagonist
Vehicle
BQ788
IRL1620
BQ123
100 µm
B
>0.9999
>0.9999
<0.0001
Axon radial length (µm)
250
200
150
100
50
0
Veh
BQ788
IRL1620
BQ123
C
0.7273
>0.9999
<0.0001
TUJ1+ area (µm2)
8000
6000
4000
2000
0
Veh
BQ788
IRL1620
BQ123
D
Harvest DRG
24 hrs
Vehicle or BQ788
7 days
NGF
Fix and Stain
12 weeks-old
(C57BL/6)
E
Vehicle
BQ788
1000 µm
F
Explant
<0.0001
Radial length (µm)
8000
6000
4000
2000
0
Veh
BQ788
G
Tuj1
Fabp7
Merged
50 µm

Fig. 3

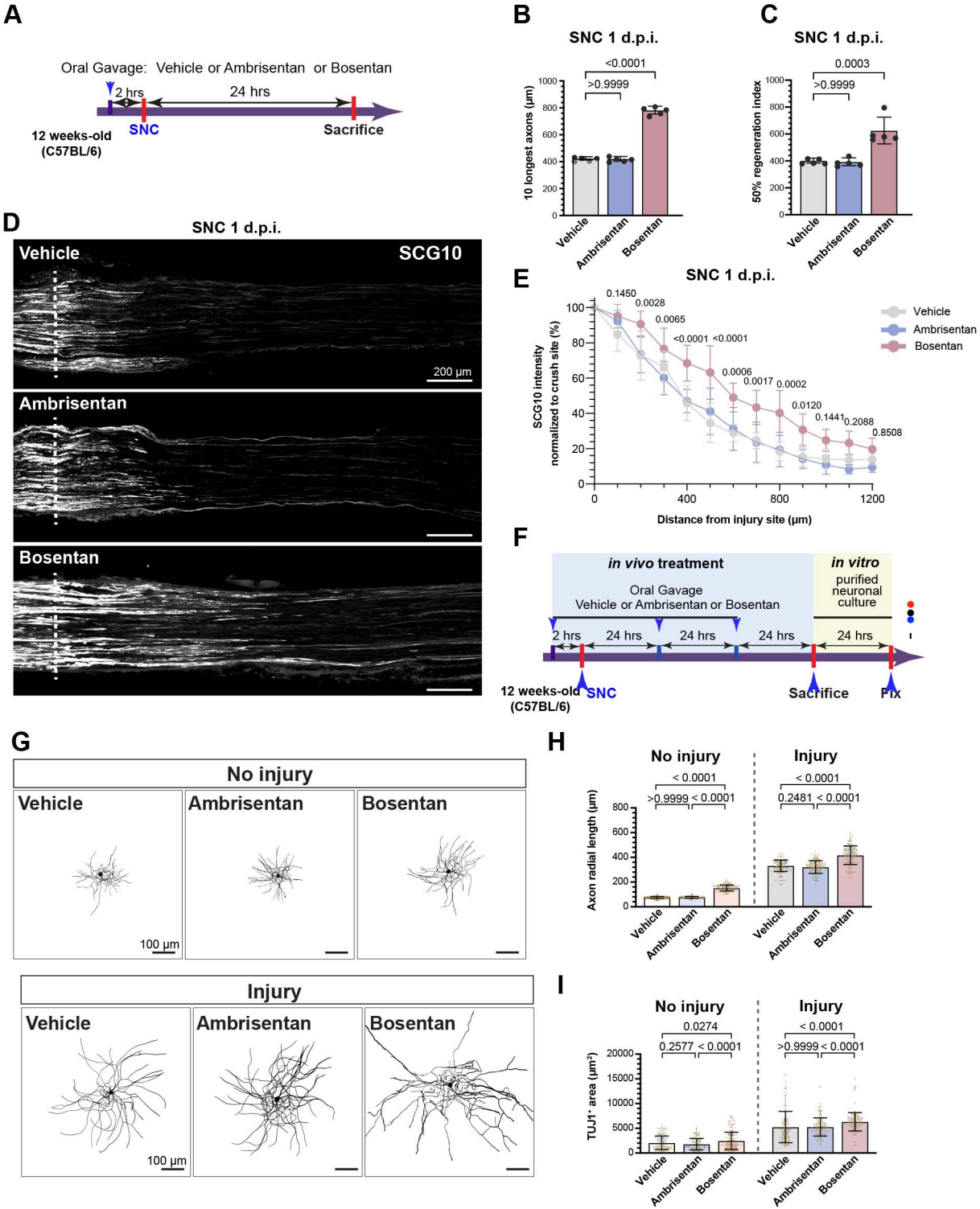
A
Oral Gavage: Vehicle or Ambrisentan or Bosentan
2 hrs
24 hrs
SNC
Sacrifice
12 weeks-old
(C57BL/6)
B
SNC 1 d.p.i.
<0.0001
>0.9999
10 longest axons (µm)
Vehicle
Ambrisentan
Bosentan
C
SNC 1 d.p.i.
0.0003
>0.9999
50% regeneration index
D
SNC 1 d.p.i.
Vehicle
SCG10
200 µm
Ambrisentan
Bosentan
E
SNC 1 d.p.i.
SCG10 intensity
normalized to crush site (%)
Distance from injury site (µm)
0.1450
0.0028
0.0065
<0.0001
<0.0001
0.0006
0.0017
0.0002
0.0120
0.1441
0.2088
0.8508
F
in vivo treatment
Oral Gavage
Vehicle or Ambrisentan or Bosentan
in vitro
purified
neuronal
culture
2 hrs
24 hrs
24 hrs
24 hrs
24 hrs
12 weeks-old
(C57BL/6)
SNC
Sacrifice
Fix
G
No injury
Vehicle
Ambrisentan
Bosentan
100 µm
Injury
Vehicle
Ambrisentan
Bosentan
100 µm
H
No injury
Injury
< 0.0001
>0.9999
< 0.0001
< 0.0001
0.2481
< 0.0001
Axon radial length (µm)
Vehicle
Ambrisentan
Bosentan
I
No injury
Injury
0.0274
0.2577
< 0.0001
< 0.0001
>0.9999
< 0.0001
TUJ1⁺ area (µm²)
Vehicle
Ambrisentan
Bosentan

Fig. 4

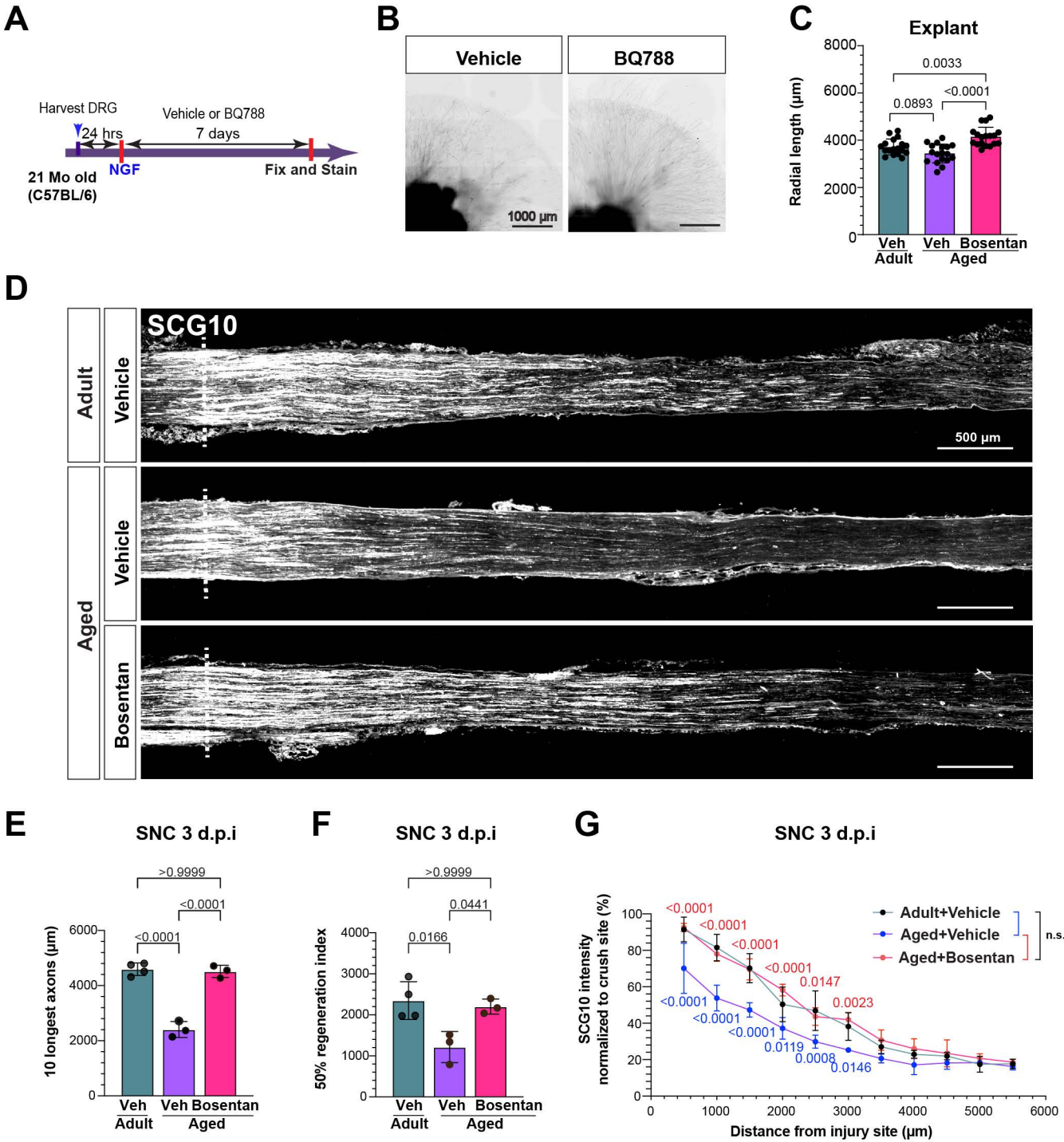
A
Harvest DRG
24 hrs
Vehicle or BQ788
7 days
NGF
Fix and Stain
21 Mo old
(C57BL/6)
B
Vehicle
BQ788
1000 µm
C
Explant
Radial length (µm)
8000
6000
4000
2000
0
0.0033
0.0893
<0.0001
Veh
Veh
Bosentan
Adult
Aged
D
SCG10
Adult
Vehicle
Aged
Vehicle
Bosentan
500 µm
E
SNC 3 d.p.i
10 longest axons (µm)
>0.9999
<0.0001
<0.0001
6000
4000
2000
0
Veh
Veh
Bosentan
Adult
Aged
F
SNC 3 d.p.i
50% regeneration index
>0.9999
0.0441
0.0166
4000
3000
2000
1000
0
Veh
Veh
Bosentan
Adult
Aged
G
SNC 3 d.p.i
SCG10 intensity
normalized to crush site (%)
Adult+Vehicle
Aged+Vehicle
Aged+Bosentan
n.s.
<0.0001
<0.0001
<0.0001
<0.0001
0.0147
0.0023
<0.0001
<0.0001
<0.0001
0.0119
0.0008
0.0146
100
80
60
40
20
0
0
1000
2000
3000
4000
5000
6000
Distance from injury site (µm)

Fig. 5

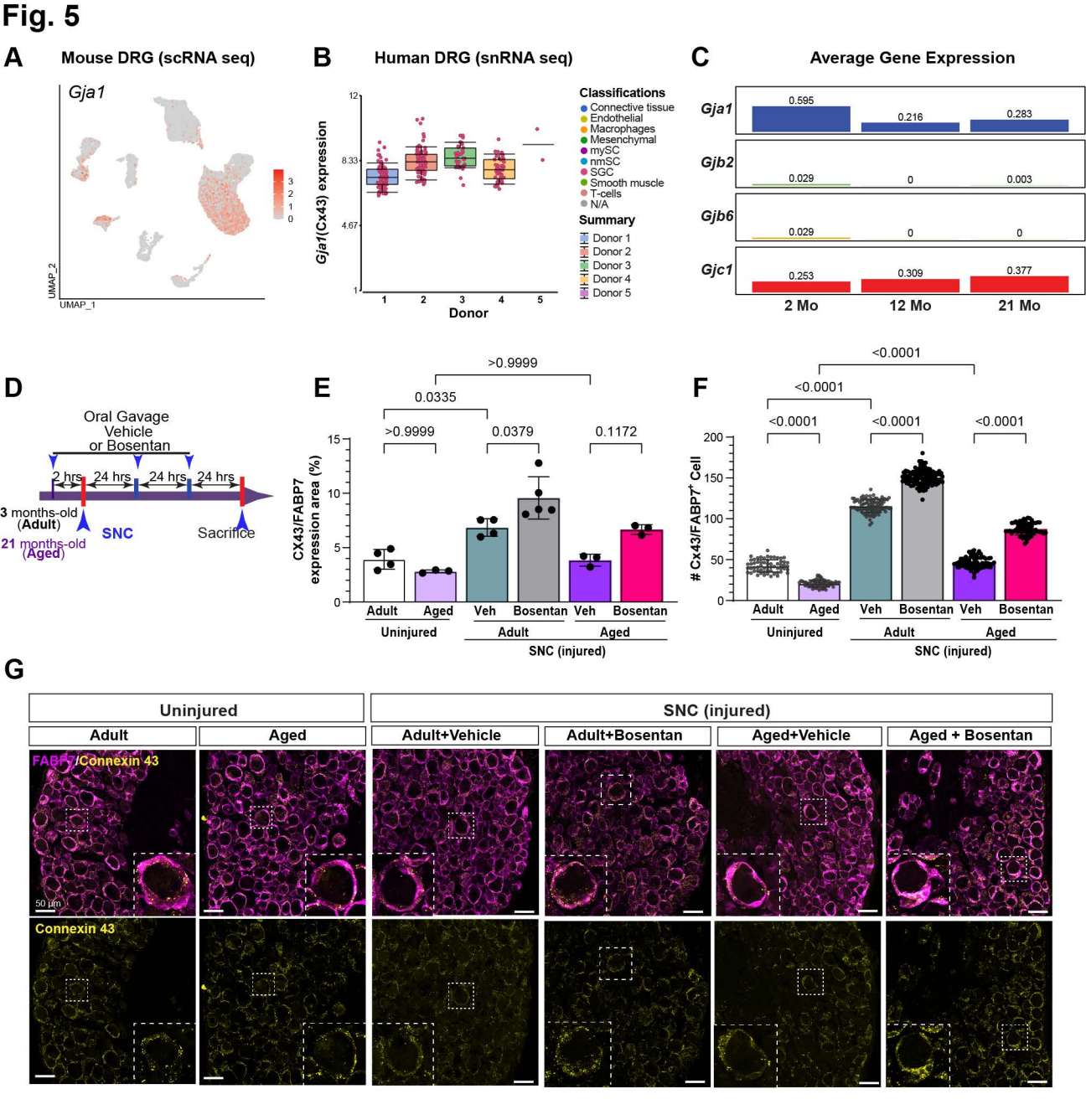
A
Mouse DRG (scRNA seq)
Gja1
UMAP_2
UMAP_1
3
2
1
0
B
Human DRG (snRNA seq)
Gja1(Cx43) expression
12
8.33
4.67
1
1
2
3
4
5
Donor
Classifications
Connective tissue
Endothelial
Macrophages
Mesenchymal
mySC
nmSC
SGC
Smooth muscle
T-cells
N/A
Summary
Donor 1
Donor 2
Donor 3
Donor 4
Donor 5
C
Average Gene Expression
Gja1
0.595
0.216
0.283
Gjb2
0.029
0
0.003
Gjb6
0.029
0
0
Gjc1
0.253
0.309
0.377
2 Mo
12 Mo
21 Mo
D
Oral Gavage
Vehicle
or Bosentan
2 hrs
24 hrs
24 hrs
24 hrs
3 months-old
(Adult)
21 months-old
(Aged)
SNC
Sacrifice
E
>0.9999
0.0335
>0.9999
0.0379
0.1172
CX43/FABP7
expression area (%)
15
10
5
0
Adult
Aged
Veh
Bosentan
Veh
Bosentan
Uninjured
Adult
Aged
SNC (injured)
F
<0.0001
<0.0001
<0.0001
<0.0001
<0.0001
Cx43/FABP7+ Cell
200
150
100
50
0
Adult
Aged
Veh
Bosentan
Veh
Bosentan
Uninjured
Adult
Aged
SNC (injured)
G
Uninjured
SNC (injured)
Adult
Aged
Adult+Vehicle
Adult+Bosentan
Aged+Vehicle
Aged + Bosentan
FABP7/Connexin 43
50 µm
Connexin 43

Fig. 6

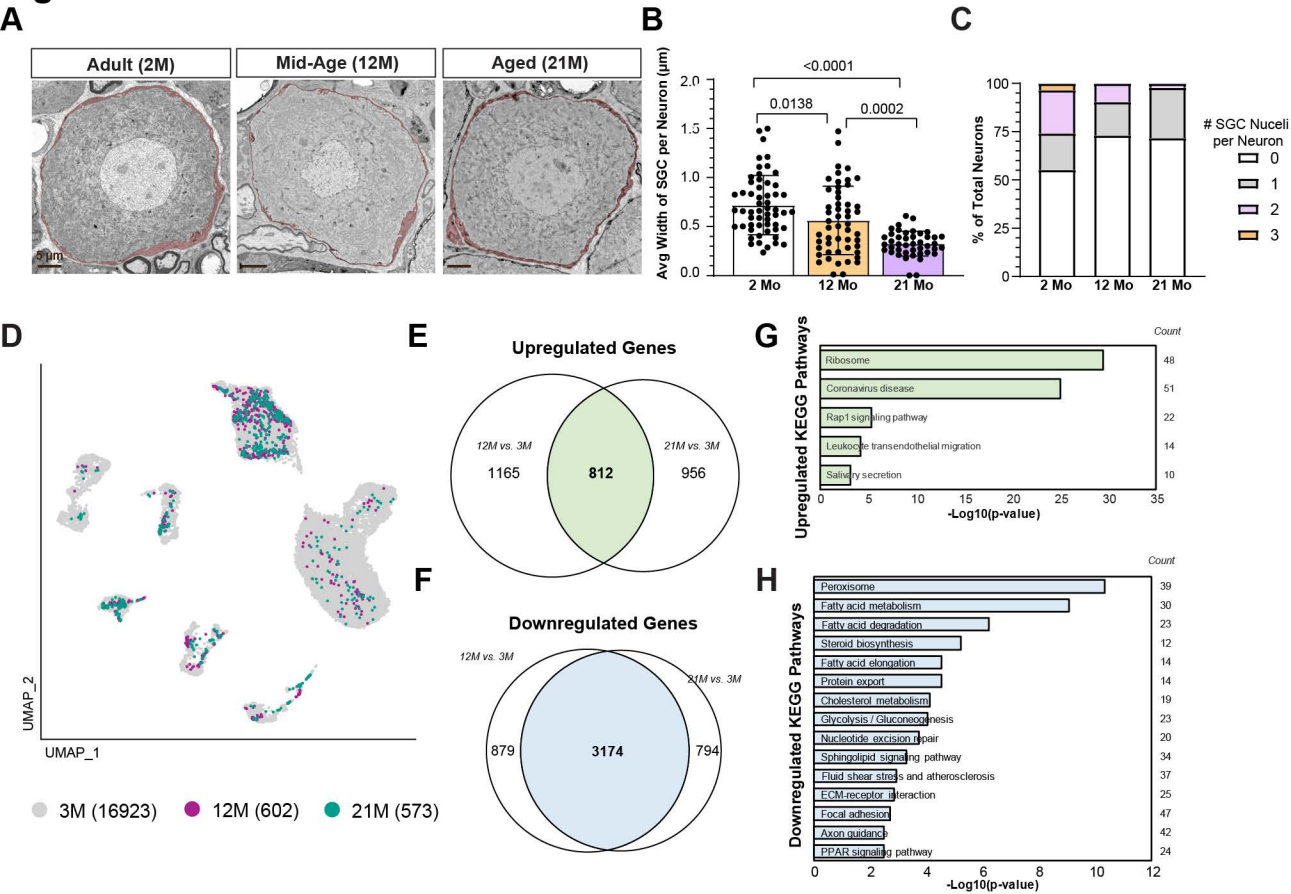
A
Adult (2M)
Mid-Age (12M)
Aged (21M)
5 µm
B
<0.0001
0.0138
0.0002
Avg Width of SGC per Neuron (µm)
2.0
1.5
1.0
0.5
0.0
2 Mo
12 Mo
21 Mo
C
% of Total Neurons
100
75
50
25
0
2 Mo
12 Mo
21 Mo
SGC Nuceli per Neuron
0
1
2
3
D
UMAP_2
UMAP_1
3M (16923)
12M (602)
21M (573)
E
Upregulated Genes
12M vs. 3M
1165
812
21M vs. 3M
956
F
Downregulated Genes
12M vs. 3M
879
3174
21M vs. 3M
794
G
Upregulated KEGG Pathways
Count
Ribosome 48
Coronavirus disease 51
Rap1 signaling pathway 22
Leukocyte transendothelial migration 14
Salivary secretion 10
0 5 10 15 20 25 30 35
-Log10(p-value)
H
Downregulated KEGG Pathways
Count
Peroxisome 39
Fatty acid metabolism 30
Fatty acid degradation 23
Steroid biosynthesis 12
Fatty acid elongation 14
Protein export 14
Cholesterol metabolism 19
Glycolysis / Gluconeogenesis 23
Nucleotide excision repair 20
Sphingolipid signaling pathway 34
Fluid shear stress and atherosclerosis 37
ECM-receptor interaction 25
Focal adhesion 47
Axon guidance 42
PPAR signaling pathway 24
0 2 4 6 8 10 12
-Log10(p-value)